A priori and a posteriori investigations for developing large eddy simulations of multi-species turbulent mixing under high-pressure conditions

Giulio Borghesi and Josette Bellan

Citation: Physics of Fluids (1994-present) **27**, 035117 (2015); doi: 10.1063/1.4916284
View online: http://dx.doi.org/10.1063/1.4916284
View Table of Contents: http://scitation.aip.org/content/aip/journal/pof2/27/3?ver=pdfcov
Published by the AIP Publishing

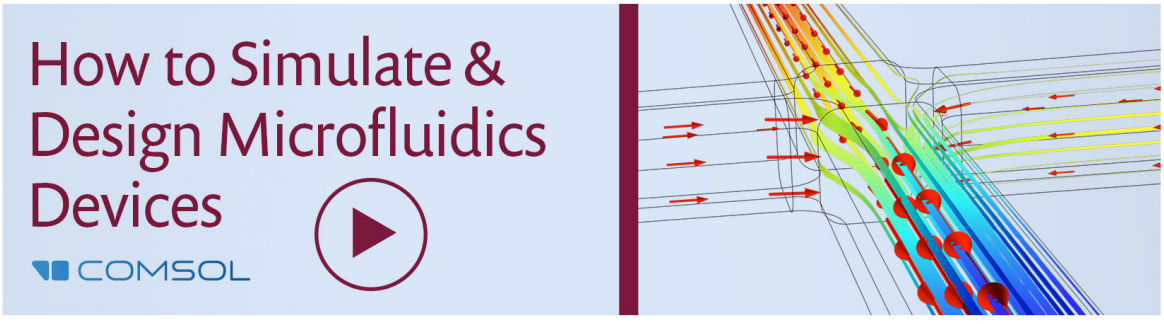

PHYSICS OF FLUIDS **27**, 035117 (2015)

A priori and *a posteriori* investigations for developing large eddy simulations of multi-species turbulent mixing under high-pressure conditions

Giulio Borghesi[1] and Josette Bellan[1,2,a)]
[1]*California Institute of Technology, Pasadena, California 91125, USA*
[2]*Jet Propulsion Laboratory, California Institute of Technology, Pasadena, California 91109-8099, USA*

(Received 4 November 2014; accepted 13 March 2015; published online 31 March 2015)

A Direct Numerical Simulation (DNS) database was created representing mixing of species under high-pressure conditions. The configuration considered is that of a temporally evolving mixing layer. The database was examined and analyzed for the purpose of modeling some of the unclosed terms that appear in the Large Eddy Simulation (LES) equations. Several metrics are used to understand the LES modeling requirements. First, a statistical analysis of the DNS-database large-scale flow structures was performed to provide a metric for probing the accuracy of the proposed LES models as the flow fields obtained from accurate LESs should contain structures of morphology statistically similar to those observed in the filtered-and-coarsened DNS (FC-DNS) fields. To characterize the morphology of the large-scales structures, the Minkowski functionals of the iso-surfaces were evaluated for two different fields: the second-invariant of the rate of deformation tensor and the irreversible entropy production rate. To remove the presence of the small flow scales, both of these fields were computed using the FC-DNS solutions. It was found that the large-scale structures of the irreversible entropy production rate exhibit higher morphological complexity than those of the second invariant of the rate of deformation tensor, indicating that the burden of modeling will be on recovering the thermodynamic fields. Second, to evaluate the physical effects which must be modeled at the subfilter scale, an *a priori* analysis was conducted. This *a priori* analysis, conducted in the coarse-grid LES regime, revealed that standard closures for the filtered pressure, the filtered heat flux, and the filtered species mass fluxes, in which a filtered function of a variable is equal to the function of the filtered variable, may no longer be valid for the high-pressure flows considered in this study. The terms requiring modeling are the filtered pressure, the filtered heat flux, the filtered pressure work, and the filtered species mass fluxes. Improved models were developed based on a scale-similarity approach and were found to perform considerably better than the classical ones. These improved models were also assessed in an *a posteriori* study. Different combinations of the standard models and the improved ones were tested. At the relatively small Reynolds numbers achievable in DNS and at the relatively small filter widths used here, the standard models for the filtered pressure, the filtered heat flux, and the filtered species fluxes were found to yield accurate results for the morphology of the large-scale structures present in the flow. Analysis of the temporal evolution of several volume-averaged quantities representative of the mixing layer growth, and of the cross-stream variation of homogeneous-plane averages and second-order correlations, as well as of visualizations, indicated that the models performed equivalently for the conditions of the simulations. The expectation is that at the much larger Reynolds numbers and much larger filter widths used in practical

a)Electronic mail: josette.bellan@jpl.nasa.gov. Tel.: 1-818-354-6959. FAX: 1-818-393-6682.

applications, the improved models will have much more accurate performance than the standard one. © *2015 AIP Publishing LLC.* [http://dx.doi.org/10.1063/1.4916284]

I. INTRODUCTION

Turbulent mixing of many species under high-pressure (high-p) conditions often occurs in combustion systems prior to ignition, in chemical engineering applications related to fluid separation, in the pharmaceutical industry, in processes involving supercritical water, and in cooling processes occurring in advanced gas turbine and scramjet engines.[1] Modeling of these general situations is highly desirable and Large Eddy Simulations (LESs) seems to be the method of choice. Recently, LESs of high-p, multi-species flows have been conducted for fuel jets[2–4] and mixing layers,[4] and also for the combustion processes occurring inside a rocket engine.[2]

The governing equations for LES of multi-species flows are obtained by applying a spatial filtering operation to the conservation equations for mass, momentum, energy, and species partial densities; the resulting equations then describe the evolution of the large-scale structures present in the flow. The influence of the small-scale structures on the dynamics of the larger ones is then represented in the LES equations by terms that are unclosed and need modeling. Two classes of unclosed terms can be identified; the conventional Subgrid Scale (SGS) fluxes, which stem from the filtering of the non-linear convective terms in the conservation equations and unconventional terms associated with the filtering of non-linear functions of the conservative variables. This latter category of terms includes the filtered pressure field $\overline{p(\phi)}$, the filtered heat flux $\overline{\mathbf{q}(\boldsymbol{\phi})}$, and the filtered species fluxes $\overline{\mathbf{J}_\alpha(\phi)}$, where ϕ is the vector of conservative variables and subscript α denotes the chemical species. While modeling of the conventional SGS fluxes has been the topic of a vast number of experimental and analytical studies since LES has first appeared, comparatively little has been done for the remaining unclosed terms. A very common approach for the modeling of $\overline{p(\phi)}$, $\overline{\mathbf{q}(\boldsymbol{\phi})}$, and $\overline{\mathbf{J}_\alpha(\phi)}$ is to assume that the difference between the filtered terms and their unfiltered counterparts, evaluated as functions of the LES solution, is small; this assumption leads to a closure of the type $\overline{f(\phi)} = f(\overline{\phi})$, where f is either p, $\mathbf{q}$, or $\mathbf{J}_\alpha$. This method has been found to be accurate for flows described by the perfect gas equation of state (EOS);[5] however, given the considerable differences that exist between the characteristics of atmospheric-p and high-p flows,[6–11] its validity for high-p flows described by real-gas equations of state has been questioned.[12–14] Indeed, in the specific context of binary-species mixing occurring at supercritical-p conditions, it has been amply demonstrated[12–14] that the closures $\overline{p(\phi)} = p(\overline{\phi})$ and $\overline{\mathbf{q}(\phi)} = \mathbf{q}(\overline{\phi})$ are no longer accurate and should be replaced in favor of better models.

For binary-species mixing, an improved closure for $\overline{p(\phi)}$ was proposed[12] and later validated.[13] This model is based on a Taylor series expansion of $p(\phi)$ in the proximity of the LES solution and requires the evaluation of the first and second derivatives of pressure with respect to the thermodynamics variables (e.g., molar volume, species molar fractions, and temperature). Although the analytical expressions for these derivatives can be easily obtained using the equation of state, the numerical implementation of the model may be costly when a large number of chemical species is present in the flow. Additionally, this model may become inaccurate and potentially unstable when a first- or second-order expansion of the pressure term is no longer sufficient for the accurate modeling of $\overline{p(\phi)}$; this may happen, for example, in the high density-gradient magnitude (HDGM) regions that characterize supercritical-p flows. Similarly, a model for the filtered heat flux was proposed[14] for binary mixing of oxygen with either helium or hydrogen, and the Approximate Deconvolution Method (ADM) was used to reconstruct solution fields ϕ^* of the conservative variables that contained the LES scales that are represented and under-resolved on the LES grid.[15] The reconstructed fields were then used to model the filtered heat flux term as $\overline{\mathbf{q}(\phi)} = \overline{\mathbf{q}(\phi^*)}$. Although an improved model for the filtered species fluxes was not deemed necessary, we note that, following the same approach used for $\overline{\mathbf{q}(\phi)}$, these terms could be modeled as $\overline{\mathbf{J}_\alpha(\phi)} = \overline{\mathbf{J}_\alpha(\phi^*)}$. An *a posteriori* study[14] of a binary-species mixing layer under supercritical-p conditions demonstrated that use of the $\overline{\mathbf{q}(\phi)} = \overline{\mathbf{q}(\phi^*)}$ model greatly improves the LES numerical predictions, especially for second-order

correlations. Despite these encouraging results, modeling of the filtered heat and species fluxes with ADM in a multiple-species context may turn out to be problematic because the reconstructed fields in ADM are obtained as linear combinations of terms of alternating signs. In regions where the solution is not sufficiently smooth, some of the reconstructed fields for the species mass fractions may become negative, and then evaluation of the diffusion coefficients and of the thermodynamics properties of the flow becomes impossible. These considerations indicate that models for $\overline{p(\phi)}$, $\overline{\mathbf{q}(\phi)}$, and $\overline{\mathbf{J}_\alpha(\phi)}$ that are of general applicability are not yet available and should therefore be sought.

The objective of this study is to propose and evaluate models for $\overline{p(\phi)}$, $\overline{\mathbf{q}(\boldsymbol{\phi})}$, and $\overline{\mathbf{J}_\alpha(\phi)}$ that can be easily implemented in LES of multi-species high-p and that are valid over a wide range of conditions. We accomplish this goal through an *a priori* analysis and an *a posteriori* assessment. To provide an additional way to probe the accuracy of the proposed LES models, a statistical analysis of the large-scale structures found in the Direct Numerical Simulation (DNS) (once transition to turbulence has occurred) is presented since it is intended that the flow fields obtained from accurate LESs should contain structures of morphology statistically similar to those observed in the filtered-and-coarsened (FC-DNS) fields.

The paper is structured as follows: The LES equations are presented in Sec. II and a description of a DNS database that was specifically created for this study follows in Sec. III. To find the morphology of the large-scale structures, we conduct a spatial statistical analysis which is presented in Sec. IV A. Foreseeing that the large-scale structures of the FC-DNS are the template for the LES, the analysis is performed both at the DNS level and for two filter widths. Then, an *a priori* analysis of the activity of the various terms in the LES equations is conducted and the results are discussed in Sec. IV B; unclosed terms with significant activity are identified and modeled. Modeling of the conventional SGS fluxes is not addressed since previous studies have already evaluated, both in the *a priori*[12] and *a posteriori*[13,14] contexts, the accuracy of these SGS flux models (e.g., Smagorinsky model, gradient model, and self-similarity model) in the supercritical-p realm. Finally, the potential of the newly proposed models for the unconventional terms to increase the accuracy of LES for supercritical-p flows is determined through an *a posteriori* assessment. A summary and conclusions are offered in Sec. V.

II. LES EQUATIONS

A. Differential LES equations

The LES conservation equations are derived from the original conservation equations through the application of a spatial filtering operation to any function $\psi(\vec{y})$ as

$$\overline{\psi}(\vec{x}) = \int_V \psi(\vec{y}) G_f(\vec{x} - \vec{y}) d\vec{y}, \tag{1}$$

where G_f is a positive filter function and V is the filtering volume;[16] G_f has the property that for a spatially invariant function, the filtered function is identical to the unfiltered one. Since the flows under consideration are compressible, Favre filtering is employed, defined as $\tilde{\psi} = \overline{\rho\psi}/\bar{\rho}$, where ρ is the density. The LES equations are written for the conservative-variable vector $\phi = \{\rho, \rho u_i, \rho e_t, \rho Y_\alpha\}$ where u_i is the ith velocity component in a Cartesian frame of reference, $e_t = e + u_i u_i/2$ is the total energy (i.e., internal energy, e, plus kinetic energy, $e_K = u_i u_i/2$), and Y_α is the mass fraction of species α,

$$\frac{\partial \overline{\rho}}{\partial t} + \frac{\partial \left(\overline{\rho}\widetilde{u_i}\right)}{\partial x_i} = 0, \tag{2}$$

$$\frac{\partial \left(\overline{\rho}\widetilde{u_i}\right)}{\partial t} + \frac{\partial \left(\overline{\rho}\widetilde{u_i}\widetilde{u_j}\right)}{\partial x_j} = -\frac{\partial \overline{p(\phi)}}{\partial x_i} + \frac{\partial \overline{\sigma_{ij}(\phi)}}{\partial x_j} - \frac{\partial \left(\bar{\rho}\tau_{ij}\right)}{\partial x_j}, \tag{3}$$

$$\frac{\partial\left(\overline{\rho}\widetilde{e_t}\right)}{\partial t}+\frac{\partial\left(\overline{\rho}\widetilde{u_j}\widetilde{e_t}\right)}{\partial x_j}=-\frac{\partial\overline{p\left(\phi\right)}\tilde{u}_j}{\partial x_j}+\frac{\partial\left(\overline{u_i\sigma_{ij}(\phi)}\right)}{\partial x_j}-\frac{\partial\overline{q_j(\phi)}}{\partial x_j}-\frac{\partial\left(\bar{\rho}\zeta_j\right)}{\partial x_j}-\frac{1}{2}\frac{\partial\left(\overline{\rho u_i u_i u_j}-\overline{\rho u_i u_i}\widetilde{u}_j\right)}{\partial x_j},$$

$$\frac{\partial\left(\overline{\rho}\widetilde{Y}_\alpha\right)}{\partial t}+\frac{\partial\left(\overline{\rho}\widetilde{u_j}\widetilde{Y}_\alpha\right)}{\partial x_j}=-\frac{\partial\left(\overline{J_{\alpha j}(\phi)}\right)}{\partial x_j}-\frac{\partial\left(\bar{\rho}\eta_{\alpha j}\right)}{\partial x_j}, \tag{4}$$

where $\alpha\in[1,N-1],N$ is the number of species, t denotes the time, subscripts i and j refer to the spatial coordinates, σ_{ij} is the Newtonian viscous stress tensor,

$$\sigma_{ij}=\mu\left(2S_{ij}-\tfrac{2}{3}S_{kk}\delta_{ij}\right),\quad S_{ij}=\frac{1}{2}\left(\frac{\partial u_i}{\partial x_j}+\frac{\partial u_j}{\partial x_i}\right), \tag{5}$$

and S_{ij} is the strain rate tensor, μ is the viscosity, and $j_{\alpha j}$ and q_j are, respectively, the αth species mass flux and the heat flux in the jth direction. τ_{ij}, ζ_j, and $\eta_{\alpha j}$ are the traditional SGS fluxes

$$\tau_{ij}=\vartheta(\widetilde{u}_i,\widetilde{u}_j),\quad \zeta_j=\vartheta(\tilde{h},\tilde{u}_j),\quad \eta_{\alpha j}=\vartheta(\widetilde{Y}_\alpha,\widetilde{u}_j)\ \text{with}\ \sum_{\alpha=1}^{N}\eta_{\alpha j}=0, \tag{6}$$

where $\vartheta(\phi,\theta)$ is defined as $\vartheta(\varphi,\theta)=\widetilde{\varphi\theta}-\widetilde{\varphi}\widetilde{\theta}$.

The expressions for the species mass fluxes and the heat flux are based on the full matrices of mass-diffusion coefficients and thermal-diffusion factors.[17–19] In detail, generically,

$$J_{\alpha j}=-\rho\left[Y_\alpha\left(D_{T,\alpha}\right)\frac{1}{T}\frac{\partial T}{\partial x_j}+Y_\alpha\left(D_{p,\alpha}\right)\frac{1}{p}\frac{\partial p}{\partial x_j}+\sum_{\beta=1}^{N-1}\left(D'_{\alpha\beta}\frac{m_\alpha}{m_\beta}\right)\frac{\partial Y_\beta}{\partial x_j}\right], \tag{7}$$

$$q_j=-\lambda\frac{\partial T}{\partial x_j}+\sum_{\alpha=1}^{N-1}J_{\alpha j}A_\alpha, \tag{8}$$

where

$$A_\alpha=\left[\left(\frac{h_\alpha}{m_\alpha}-\frac{h_N}{m_N}\right)-R_uT\left(\frac{\bar{\alpha}^b_{T,\alpha}}{m_\alpha}-\frac{\bar{\alpha}^b_{T,N}}{m_N}\right)\right]. \tag{9}$$

The consideration of the set of $(N-1)$ species equations rather than the set of N dependent species ensures that the equations are independent; in these $(N-1)$ equations, the original species mass fluxes and the heat flux were rewritten to account for only $(N-1)$ gradients. In Eqs. (7)–(9),

$$D_{T,\alpha}=-\sum_{\beta=1}^{N}\bar{\alpha}^b_{T,\beta}\mathbb{D}_{\beta\alpha},\qquad D_{p,\alpha}=\frac{p}{R_uT}\sum_{\beta=1}^{N}v_\beta\mathbb{D}_{\beta\alpha}, \tag{10}$$

$$D_{\alpha\gamma}=\sum_{\beta=1}^{N}\mathbb{D}_{\alpha\beta}\alpha_{D\beta\gamma}, \tag{11}$$

$$\bar{\alpha}^b_{T,\alpha}=\sum_{\beta=1}^{N}X_\beta\alpha^b_{T,\beta\alpha}, \tag{12}$$

$$D'_{\alpha\beta}=D_{\alpha\beta}-\left(1-\frac{m_\beta}{m_N}\right)\left(\sum_{\gamma=1}^{N-1}D_{\alpha\gamma}X_\gamma\right). \tag{13}$$

Here, $X_\alpha=Y_\alpha m/m_\alpha$ represents the molar fraction; m_α is the species molar mass; m is the mixture molar mass, $m=\sum_{\gamma=1}^{N}m_\gamma X_\gamma$; $v_\alpha=(\partial v/\partial X_\alpha)_{T,p,X_{\beta(\beta\neq\alpha)}}$ is the partial molar volume, where the molar volume is $v=m/\rho$; $h_\alpha=(\partial h/\partial X_\alpha)_{T,p,X_{\beta(\beta\neq\alpha)}}$ is the partial molar enthalpy, where the molar enthalpy is $h=G-T(\partial G/\partial T)_{p,X}$ with G being the Gibbs energy; R_u is the universal gas constant; $D_{\alpha\gamma}$ are the pairwise mass diffusion coefficients; and $\alpha^b_{T,\alpha\beta}$ are the binary thermal diffusion factors. The mass-diffusion factors, $\alpha_{D\alpha\beta}$, are calculated from thermodynamics as

$$\alpha_{D\alpha\beta}\equiv\frac{1}{R_uT}X_\alpha\frac{\partial\mu_\alpha}{\partial X_\beta}=(\delta_{\alpha\beta}-\delta_{\alpha N})+X_\alpha(R_{\alpha\beta}-R_{\alpha N}),\quad 1\leqslant\alpha\leqslant N,\ 1\leqslant\beta\leqslant N-1, \tag{14}$$

$$R_{\alpha\beta} \equiv \frac{\partial \ln \gamma_\alpha}{\partial X_\beta}, \quad 1 \leqslant \alpha \leqslant N,\ 1 \leqslant \beta \leqslant N, \tag{15}$$

where μ_α is the chemical potential of species α written in terms of $N-1$ species; $\gamma_\alpha \equiv \varphi_\alpha/\varphi_\alpha^o$, where φ is the fugacity coefficient written in terms of N species and the superscript o denotes the pure ($X_\alpha = 1$) limit. Matrix elements $\mathbb{D}_{\beta\gamma}$ are the solution of the mixing rules equations,[18]

$$\sum_{\beta=1}^{N} \left[\delta_{\alpha\beta} - \left(1-\delta_{\alpha\beta}\right) X_\beta \frac{\bar{\mathcal{D}}_\alpha}{\mathcal{D}^b_{\alpha\beta}} \right] \frac{\mathbb{D}_{\beta\gamma}}{X_\beta} = \bar{\mathcal{D}}_\alpha \frac{\left(\delta_{\alpha\gamma} - Y_\alpha\right)}{X_\alpha}, \tag{16}$$

where

$$\bar{\mathcal{D}}_\alpha = 1/\sum_{\substack{\beta=1 \\ \beta\neq\alpha}}^{N} \left(\frac{X_\beta}{\mathcal{D}^b_{\alpha\beta}} \right). \tag{17}$$

Solutions for $\mathbb{D}_{\beta\gamma}$ may be obtained by an approximate inversion[20] as follows:

$$\mathbb{D}_{\beta\gamma} \simeq X_\beta \mathbb{D}^{(1)}_{\beta\gamma}, \tag{18}$$

$$\mathbb{D}^{(1)}_{\alpha\beta} = \frac{\left(1+Y_\alpha\right)}{X_\alpha} \mathcal{D}^*_\alpha \delta_{\alpha\beta} + \left(1-\delta_{\alpha\beta}\right) \frac{\mathcal{D}^*_\alpha \mathcal{D}^*_\beta}{\mathcal{D}^b_{\alpha\beta}} - \left(\sigma_\alpha \mathcal{D}^*_\alpha + \sigma_\beta \mathcal{D}^*_\beta\right) + \sum_{\gamma=1}^{N} \left(Y_\gamma \sigma_\gamma \mathcal{D}^*_\gamma\right), \tag{19}$$

$$\mathcal{D}^*_\alpha = \left(1-Y_\alpha\right) \bar{\mathcal{D}}_\alpha, \tag{20}$$

$$\sigma_\alpha = \frac{m_\alpha}{m}\left(1+Y_\alpha\right) + \sum_{\substack{\beta=1 \\ \beta\neq\alpha}}^{N} Y_\beta \frac{\mathcal{D}^*_\beta}{\mathcal{D}^b_{\alpha\beta}}, \tag{21}$$

where $\mathcal{D}^b_{\alpha\beta}$ is the full approximation binary-diffusion matrix. This inter-species diffusion model, Eqs. (17)–(21), is not valid when the mixture is composed of a single species (as, for instance, in pure fuel zones). In that case, Eq. (17) is no longer used and the diffusion coefficients are evaluated using the binary-diffusion matrix by setting $\mathcal{D}^*_\alpha = \mathcal{D}^b_{\alpha N}$, where N represents the index associated with the solvent. This method was tested against an exact Gauss inversion and it gave the same results, with an additional gain in computational time. Defining $\mathcal{D}_{\alpha\beta}$ as the first approximation of the binary diffusion matrix and realizing that the deviation of the ratio $\mathcal{D}^b_{\alpha\beta}/\mathcal{D}_{\alpha\beta}$ from unity is comparable to uncertainties in binary diffusion coefficients values,[18] we assume $\mathcal{D}^b_{\alpha\beta} = \mathcal{D}_{\alpha\beta}$. The computation of the mixture physical viscosity, μ_{ph}, of the mixture physical thermal conductivity of λ_{ph}, of $\mathcal{D}_{\alpha\gamma}$, and of $\alpha^b_{T,\alpha\gamma}$ is presented in Appendix A.

B. The equation of state

Differential Eqs. (2)–(4) are coupled to the Peng-Robinson (PR) EOS given by the generic relationship

$$p(\phi) = \frac{R_u T(\phi)}{\left(v_{\mathrm{PR}}(\phi) - b_{\mathrm{mix}}(\phi)\right)} - \frac{a_{\mathrm{mix}}(\phi)}{\left(v^2_{\mathrm{PR}}(\phi) + 2b_{\mathrm{mix}}(\phi)v_{\mathrm{PR}}(\phi) - b^2_{\mathrm{mix}}(\phi)\right)}, \tag{22}$$

where v_{PR} is the molar PR volume and $v = v_{\mathrm{PR}} + v_s$, with v_s being a volume shift introduced so as to improve the accuracy of the PR EOS at high p; the v_s computation was explained in detail elsewhere.[9] The expressions for a_{mix} and b_{mix} are highly nonlinear functions of T and X_i (see Appendix B for details).

C. Unclosed terms appearing in the LES equations

The LES equations of Sec. II A contain terms that are unclosed and need modeling. Two types of unclosed terms can be identified: the conventional SGS fluxes τ_{ij}, ζ_j, and $\eta_{\alpha j}$, which stem from the non-linear nature of the convective terms and those obtained when filtering the remaining

non-linear terms in the governing equations. The terms belonging to this last category are the following:

$$\overline{p(\phi)}, \quad \overline{\sigma_{ij}(\phi)}, \quad \overline{u_i\sigma_{ij}(\phi)}, \quad \overline{q_j(\phi)}, \quad \overline{J_{\alpha j}(\phi)}, \quad \text{and} \quad \frac{1}{2}\frac{\partial\left(\overline{\rho u_i u_i u_j} - \overline{\rho u_i u_i}\widetilde{u_j}\right)}{\partial x_j}. \tag{23}$$

The last term in Eq. (23) appears only in the energy equation and can be split in two contributions,

$$\frac{\partial\left(\overline{\rho u_i u_i u_j} - \overline{\rho u_i u_i}\widetilde{u_j}\right)}{\partial x_j} = \frac{\partial\overline{\rho}\left(\kappa_j - \tau_{ij}\right)}{\partial x_j} + \frac{\partial\overline{\rho}\tau_{ij}}{\partial x_j}, \quad \text{with} \quad \kappa_j = \vartheta(\widetilde{e}_K, \widetilde{u}_j). \tag{24}$$

This term is usually negligible for low-Mach number flows, as demonstrated in Sec. IV B 1.

Modeling of the conventional SGS fluxes has received the most attention in the LES literature, whereas simplistic assumptions have been usually employed for the remaining unclosed terms. A popular approach, which will be referred to in the remainder of this paper as the "standard LES assumption" (SLA), is to evaluate these terms by assuming that $\overline{f(\phi)} = f(\overline{\phi})$, where f indicates a generic function of ϕ. According to the SLA,

$$\begin{aligned}
&\overline{p(\phi)} = p(\overline{\phi}),\\
&\overline{\sigma_{ij}(\phi)} = \sigma_{ij}(\overline{\phi}), \quad \overline{u_i\sigma_{ij}(\phi)} = \widetilde{u}_i\sigma_{ij}(\overline{\phi}),\\
&\overline{q_j(\phi)} = q_j(\overline{\phi}), \quad \text{and} \quad \overline{J_{\alpha j}(\phi)} = J_{\alpha j}(\overline{\phi}).
\end{aligned} \tag{25}$$

The above approximations are valid when the ambient pressure is sufficiently low and the perfect gas equation of state can be used; however, they may not be accurate when flows under supercritical-pressure conditions are considered. This is particularly true for $\overline{p(\phi)}$, $\overline{q_j(\phi)}$, and $\overline{J_{\alpha j}(\phi)}$. For the sake of further analysis, it is convenient to rewrite each of the terms in Eq. (23) as the sum of a resolved part and a SGS contribution,

$$\begin{aligned}
&\overline{p(\phi)} = p(\overline{\phi}) + \left(\overline{p(\phi)} - p(\overline{\phi})\right),\\
&\overline{\sigma_{ij}(\phi)} = \sigma_{ij}(\overline{\phi}) + \left(\overline{\sigma_{ij}(\phi)} - \sigma_{ij}(\overline{\phi})\right), \quad \overline{u_i\sigma_{ij}(\phi)} = \widetilde{u}_i\sigma_{ij}(\overline{\phi}) + \left(\overline{u_i\sigma_{ij}(\phi)} - \widetilde{u}_i\sigma_{ij}(\overline{\phi})\right),\\
&\overline{q_j(\phi)} = q_j(\overline{\phi}) + \left(\overline{q_j(\phi)} - q_j(\overline{\phi})\right), \quad \overline{J_{\alpha j}(\phi)} = J_{\alpha j}(\overline{\phi}) + \left(\overline{J_{\alpha j}(\phi)} - J_{\alpha j}(\overline{\phi})\right).
\end{aligned} \tag{26}$$

The terms in the LES equations involving the quantities listed in Eq. (23) can then be rewritten as follows:

Momentum equation:

$$\frac{\partial\overline{p(\phi)}}{\partial x_i} = \frac{\partial p(\overline{\phi})}{\partial x_i} + \frac{\partial\left(\overline{p(\phi)} - p(\overline{\phi})\right)}{\partial x_i}, \quad \frac{\partial\overline{\sigma_{ij}(\phi)}}{\partial x_j} = \frac{\partial\sigma_{ij}(\overline{\phi})}{\partial x_j} + \frac{\partial\left(\overline{\sigma_{ij}(\phi)} - \sigma_{ij}(\overline{\phi})\right)}{\partial x_j}.$$

Energy equation:

$$\begin{aligned}
&\frac{\partial\overline{u_i\sigma_{ij}(\phi)}}{\partial x_j} = \frac{\partial\widetilde{u}_i\sigma_{ij}(\overline{\phi})}{\partial x_j} + \frac{\partial\left(\overline{u_i\sigma_{ij}(\phi)} - \widetilde{u}_i\sigma_{ij}(\overline{\phi})\right)}{\partial x_j}, \quad \frac{\partial\overline{q_j(\phi)}}{\partial x_j} = \frac{\partial q_j(\overline{\phi})}{\partial x_j} + \frac{\partial\left(\overline{q_j(\phi)} - q_j(\overline{\phi})\right)}{\partial x_j},\\
&\frac{\partial\overline{p(\phi)}\widetilde{u}_j}{\partial x_j} = \frac{\partial p(\overline{\phi})\widetilde{u}_j}{\partial x_j} + \frac{\partial\left(\overline{p(\phi)}\widetilde{u}_j - p(\overline{\phi})\widetilde{u}_j\right)}{\partial x_j}.
\end{aligned}$$

Species equation:

$$\frac{\partial\overline{J_{\alpha j}(\phi)}}{\partial x_j} = \frac{\partial J_{\alpha j}(\overline{\phi})}{\partial x_j} + \frac{\left(\overline{J_{\alpha j}(\phi)} - J_{\alpha j}(\overline{\phi})\right)}{\partial x_j}. \tag{27}$$

This form is useful in that it allows to assess the accuracy of the SLAs in an easy and straightforward way. If these assumptions were accurate, the SGS terms in Eq. (27) would be null.

TABLE I. Species properties. The species are listed in order of index α. v is the molar volume, Ω is the acentric factor, and subscript c denotes the critical point.

Species	Species label (α)	m_α (kg/kmol)	T_c (K)	p_c (bar)	v_c ($\frac{10^{-3}\ \mathrm{m}^3}{\mathrm{kmol}}$)	Ω
H_2O	1	18.015	647.3	221	57.1	0.344
CO_2	2	44.01	304.1	73.8	93.9	0.239
O_2	3	32.0	154.6	50.43	73.4	0.025
C_7H_{16}	4	100.2	540.2	27.4	432	0.349
N_2	5	28.013	126.26	33.4	89.8	0.039

III. DESCRIPTION OF THE DNS DATABASE

The simulations describe the mixing between two streams having different chemical compositions; the five species selected for the simulations are relevant to combustion. The fuel is represented by n-C_7H_{16} because it is representative of diesel fuel; air is represented by its major species, that is, N_2 and O_2; and the major products of complete combustion are CO_2 and H_2O. The properties of these species are listed in Table I and the initial composition of the two streams is provided in the caption of Table II. n-C_7H_{16} and O_2 will be referred to as "major species" since they are present in abundance in either the upper or the lower stream; conversely, CO_2 and H_2O will be labeled "minor species" since their mass fractions are initially small in the entire mixing layer.

For specific use in the present study, we created two DNS realizations employing the molecular fluxes' model described in a previous study[7] and we focussed on investigating the influence of the freestream pressure, p_0. The DNSs were performed in a temporal mixing layer configuration having periodic boundary conditions in the streamwise (x_1) and spanwise (x_3) directions, and non-reflecting boundary conditions in the cross-stream (x_2) direction.[21] The mixing layer initially hosted four spanwise vortices and the initial vorticity was perturbed to accelerate the roll-up and successive pairing of the vortices, leading to an ultimate vortex. In contrast to the DNSs created in our previous multi-species study,[7] the mean flow and the initial perturbation used in our previous binary-species study[8] were adopted because the resulting flow field displays a thicker mixing layer early during the simulation, a fact which enabled obtaining a high-quality simulation on a coarser grid compared to our previous multi-species study.[7] The domain size in the streamwise (L_1) and spanwise (L_3) directions is such that it accommodates initially four vortices associated with the wavelengths λ_1 and λ_3 of perturbations,[8] respectively. The domain lengths, L_i ($i = [1,3]$), were the same for all simulations and are listed in the caption of Table II. The cross-stream domain size (L_2) is large enough so that there is no interference of the mixing region with the domain boundaries.

The initial Reynolds number was defined as $\mathrm{Re}_0 \equiv \left[0.5(\rho_U + \rho_L)\Delta U_0 \delta_{\omega,0}\right]/\mu_R$, where ρ_U and ρ_L are the mixture initial densities, with subscripts U and L labeling the upper and lower streams, respectively; $\delta_{\omega,0} = \Delta U_0/(\partial \langle u_1 \rangle / \partial x_2)_{max}$ is the initial vorticity thickness, where $\langle\cdot\rangle$ represents the (x_1, x_3) planar average; $\Delta U_0 = U_U - U_L$ is the initial velocity difference across the layer; and μ_R is a reference viscosity. To compute μ_R, first a physical initial-mixture viscosity $\mu_{ph,0}$ was computed

TABLE II. List of the direct numerical simulation realizations and associated resolution. L_i is the size of the domain in the x_i direction, in meters. For both DNSs, $\mathrm{Re}_0 = 1000$, $L_1 = 0.2$ m, $L_2 = 0.1778$ m, and $L_3 = 0.12$ m; $T_U = 1000$ K and $T_L = 600$ K. The initial composition in the upper stream is $Y_{H_2O} = 0.01$, $Y_{CO_2} = 0.035$, $Y_{O_2} = 0.2$, $Y_{C_7H_{16}} = 0$, and $Y_{N_2} = 0.755$, and in the lower stream is $Y_{H_2O} = 0.01$, $Y_{CO_2} = 0.035$, $Y_{O_2} = 0$, $Y_{C_7H_{16}} = 0.955$, and $Y_{N_2} = 0$. The amplitudes of the initial vorticity perturbation are $F_{3D} = 0.08$ and $F_{2D} = 0.05$ in the streamwise and spanwise directions, respectively. The computational grid was $540 \times 480 \times 324$ and the grid spacing was 3.70×10^{-4} m.

Run	p_0 (atm)	$\left(\frac{\rho_L}{\rho_U}\right)_0$	$\mathrm{Re}_{m,tr}$	t^*_{tr}
p60	60	9.68	1741	112
p80	80	10.03	1698	108

based on the physical initial species viscosities (Appendix A), then a reference value μ_R was obtained from the chosen Re_0, and finally a factor $\mathcal{FA} \equiv \mu_R/\mu_{ph,0}$ was defined. All physical transport properties computed according to the methods explained in Appendix A were then scaled by $\mathcal{FA}$, a procedure which allowed the computation of accurate dimensionless numbers. The value of $\mathcal{FA}$ was computed at the initial time, for the initial constant p_0 and $T_0 = (T_U + T_L)/2$, using the 5-species mixture, each species being averaged over the entire domain. In this way, a unique $\mathcal{FA}$ value was employed in the computational domain. This scaling satisfies the Batchelor principle of flow similarity[22] stating that flow characteristics only depend upon non-dimensional numbers rather than individual transport properties. As done previously,[9] an initial convective Mach number was specified, $Ma_0 = 0.4$, which together with the speed of sound and the compressibility factor computed from the EOS determined the values of U_U and U_L.

The computational methodology has already been described in detail[7] and thus will only be summarized here. The differential equations were discretized using a sixth-order compact scheme and time integration was performed utilizing a fourth-order explicit Runge-Kutta time scheme. Time stability was obtained by filtering the conservative variables every five time steps employing an eighth-order explicit filter.[23] The computations were parallelized using three-dimensional domain decomposition and message passing interface; the tridiagonal solver for the spatial discretization scheme was efficiently parallelized.[24] p and T were computed from the EOS and the known functional dependence of e on (T,p) using an iterative scheme. The grid spacing, Δx, was uniform and was selected to ensure that the smallest scales relevant to dissipation were resolved. The computations were stopped at a transitional state identified by the first time at which the spectra for the dynamic and thermodynamic variables were smooth, thereby showing the characteristics of turbulence; the corresponding non-dimensional time was labeled t^*_{tr}, where $t^* \equiv t\Delta U_0/\delta_{\omega,0}$. The excellent resolution is demonstrated in Fig. 1 showing the fluctuation-based spectra for $\mathbf{u}$, T and Y_α for each simulation at t^*_{tr}.

The names of the simulations, p60 and p80, and the database's characteristics are listed in Table II where the values of relevant quantities, including t^*_{tr}, are provided. An indication of the turbulence level achieved at transition is given by $\mathrm{Re}_m = \mathrm{Re}_0\, \delta_{m,\mathrm{tr}}/\, \delta_{\omega,0}$, where δ_m is the momentum thickness,

$$\delta_m = \frac{\int_{x_{2,\min}}^{x_{2,\max}} \left[\langle \rho u_1\rangle_{x_2,\max} - \langle \rho u_1\rangle\right]\left[\langle \rho u_1\rangle - \langle \rho u_1\rangle_{x_2,\min}\right] dx_2}{\left(\langle \rho u_1\rangle_{x_2,\max} - \langle \rho u_1\rangle_{x_2,\min}\right)^2}. \tag{28}$$

In the above equation, $x_{2,\min} = -L_2/2.5$ and $x_{2,\max} = x_{2,\min} + L_2$. The values of Re_m for the simulations presented in this study are provided in Table II.

IV. RESULTS

Time-averaged results are not statistically significant in the present study since the mixing layers are unsteady; and it is well known that systems potentially containing several phases (as could be the case under high-pressure conditions) are not ergodic[25] because one or several order parameters—i.e., additional variables—must be provided to describe the state of the system,[26] particularly when there is a possibility of being near the critical point where large thermodynamic fluctuations exist. Moreover, we already know that the flows of present interest have distinct inhomogeneities,[6–11] in which case duplicating the local aspect of the flow may be important. Indeed, local inhomogeneities affect turbulence production[7,27] as well as phase separation.[26,28,29] These arguments lead to the analysis being focussed on the state obtained at t^*_{tr}.

In analyzing the numerical results, we first perform a statistical analysis of the large-scale distortion of the mixing layers at t^*_{tr}. The scope of this analysis is to identify the geometrical and morphological properties of the large-scale structures in the flows and provide one of several measures to evaluate the success of the LES models in the *a posteriori* study.

Next, we conduct an *a priori* analysis in which we examine the relative importance of the terms appearing in the LES equation at t^*_{tr}. As part of the *a priori* analysis, models for those unclosed terms that are found to be non-negligible are then formulated and assessed using data extracted

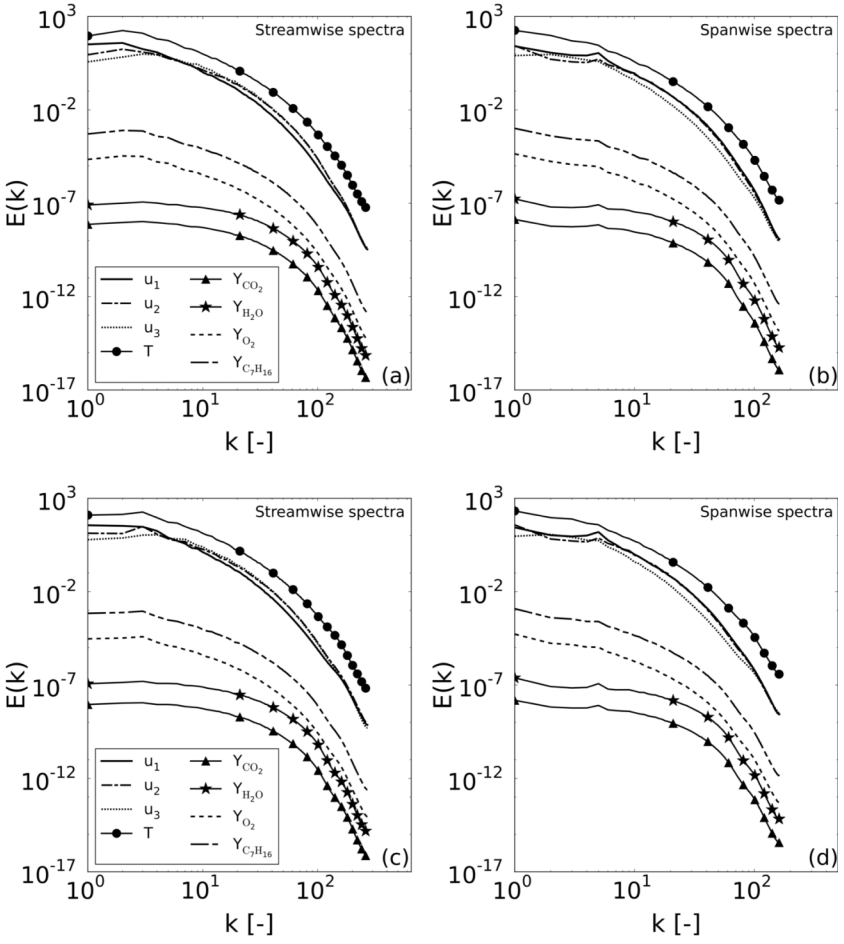

FIG. 1. One-dimensional spectra at t^*_{tr}: (a) streamwise for p60; (b) spanwise for p60; (c) streamwise for p80; and (d) spanwise for p80.

from the DNS database. The attention is focused here on the unconventional SGS terms given in Eq. (27). No new models for the conventional SGS terms τ_{ij}, ζ_j, and $\eta_{\alpha j}$ are proposed here since, as already stated in Sec. I, equivalent studies[12–14] exist for binary-species mixing under supercritical-p conditions, and these findings are expected to hold here as well due to the convective nature of the conventional SGS fluxes.

To evaluate the proposed LES models for the unconventional SGS terms, an *a posteriori* investigation is finally conducted. The accuracy of the various LES models is assessed by comparing the LES and FC-DNS solutions from the viewpoints of (i) the statistical geometrical and morphological aspects of the large-scale structures in the flows; (ii) the predictions of integral quantities; (iii) the results obtained for the homogeneous-plane averages of the velocity, thermodynamic variables, and second-order correlations; and (iv) visualizations.

In performing both the *a priori* and the *a posteriori* studies, the DNS data must be filtered; to this scope, a top-hat filter is used, being the only one consistent with easy interpretation of results when using a finite difference scheme. Two LES filter widths are considered, $\overline{\Delta} = 3\Delta x$ and $\overline{\Delta} = 6\Delta x$, these values being representative of two coarse-grid LESs. Since the analysis is performed on transitional rather than fully turbulent flows, a coarse-grid LES is obtained at considerably smaller $\overline{\Delta}$ than in fully turbulent flows. Indeed, what determines the fine-grid versus the coarse-grid LES regimes is not the value of the ratio between $\overline{\Delta}$ and the smallest scale, but rather the effects captured when filtering at that $\overline{\Delta}$; the fine-grid LES is only concerned with SGS models for dissipation whereas the coarse-grid LES will contain SGS effects others than those of dissipation. In

fully turbulent flows, the dissipation range can be considered to be $\sim 10l$, where l is the smallest flow scale. For fully turbulent flows, any $\overline{\Delta}$ within $10l$ can be considered to correspond to fine-grid LES. For a fully turbulent flow, coarse-grid LES is considered to start at the inertial subrange and the characteristic of this range is that additional to the dissipation effects, larger scale activity must also be modeled. As will be seen below, even at $\overline{\Delta} = 3\Delta x$, the present filtered flow field contains significant effects other than those of dissipation and thus qualifies as coarse-grid LES. Also, both for fully turbulent and transitional flows, the inertial range corresponds to the spectral range having the $-5/3$ slope. For fully turbulent flows, the dissipation range exhibits a drastic drop-off in slope; between the inertial range and the dissipation range, there is a range with an intermediary slope, and this is the scale-similarity regime. But for transitional flows, the dissipation range is not well marked because the slope drop-off does not occur; in fact, the slope in the high-wavenumber regime is somewhere between that of the scale-similarity range of fully turbulent flows and of the dissipation range of fully turbulent flows. That is, while we know for these transitional flows that the smallest scale reached is that of dissipation, the scale-similarity regime can be very close to that of the dissipation since the separation of scales is not well marked.[16] Our study takes full advantage of these two beneficial aspects of transitional flows, i.e., reaching a coarse-grid LES and scale similarity close to the dissipation range, for model development.

A. Statistical analysis of flow characteristics at t^*_{tr}

High-p turbulent flows undergoing multiple-species mixing are characterized by several structural features, among which one of the most important is the occurrence of HDGM regions.[10,11] Accurate LES would reproduce the salient properties of these flows, meaning that not only spatially averaged values and rms of several fluid-dynamics variables, such as the velocity components, would be captured but also that the spatial statistical occurrence of large-scale structures within the flow would be correctly represented. To characterize the large-scale distortion of a turbulent flow, we examine the spatial distributions of two important quantities: the second invariant of the rate of deformation tensor,[30] II_d, which addresses the dynamic aspects of the flow, and the irreversible entropy production rate g, which primarily addresses the thermodynamics.[7] II_d is chosen here rather than other variables because it provides both shape change and rotation information regarding material elements. This quantity is preferable to the strain rate tensor, which only addresses the shape change, and also to the rotation rate tensor, which lacks information on the elements shapes. g is the sum of the contributions responsible for entropy production due to species diffusion, heat conduction, and viscous dissipation. This quantity is useful from the viewpoint of turbulent combustion modeling as it highlights those regions of the flow where strong mixing occurs.

These structural features can be studied using a Minkowski functionals' (MFs) analysis. In conducting the MF analysis, the DNS solution is filtered and coarsened to remove the small scales structures using either $\overline{\Delta} = 3\Delta x$ or $\overline{\Delta} = 6\Delta x$; the FC-DNS fields are then used to compute II_d and g. Then, the MFs of selected iso-surfaces of II_d and g are evaluated.

1. Introduction to MFs

The MFs[31–34] are Galilean invariant morphological properties of a surface derived from integral geometry theory. In a three-dimensional space, four MFs can be defined. Following previously defined notation,[33,34]

$$V,\ S,\ C = \frac{1}{2}\oint\left(\frac{1}{R_1}+\frac{1}{R_2}\right)dS,\ \chi = \frac{1}{2\pi}\oint\left(\frac{1}{R_1R_2}\right)dS, \tag{29}$$

where V is the volume enclosed by the surface associated with the MF, S is its area, and C and χ are, respectively, the integrated mean curvature and the "integrated Gaussian curvature" (or Euler characteristic) of the surface. A quantity linked to the integrated Gaussian curvature is the genus

$$\mathcal{G} = 1 - \frac{\chi}{2}, \tag{30}$$

which can be interpreted as the number of independent cuts that a surface can sustain without being broken into separate pieces. From the MFs, three additional quantities, called "shapefinders," can be defined:[31–34] these are the "thickness" $\mathcal{T}$, the "breadth" $\mathcal{B}$, and the "length" $\mathcal{L}$,

$$\mathcal{T} = \frac{3V}{S}, \quad \mathcal{B} = \frac{S}{C}, \quad \mathcal{L} = \frac{C}{4\pi\mathcal{G}}. \tag{31}$$

Two dimensionless shapefinders, named "planarity" $\mathcal{P}$ and "filamentarity" $\mathcal{F}$, can then be obtained by combining the above shapefinders,

$$\mathcal{P} = \frac{\mathcal{B}-\mathcal{T}}{\mathcal{B}+\mathcal{T}}, \quad \mathcal{F} = \frac{\mathcal{L}-\mathcal{B}}{\mathcal{L}+\mathcal{B}}. \tag{32}$$

These quantities and the genus are sufficient to characterize the topology and morphology of a surface. Clearly, before computing $(\mathcal{P},\mathcal{F},\mathcal{G})$, one must identify the surfaces to be probed. The construction of the iso-surfaces is here performed using an enhanced version[35] of the marching cube algorithm[36] while the MFs are computed following a previously described procedure.[33] Only the $\mathcal{G} = 0$ iso-surfaces are considered in our analysis; this choice implies that both the planarity and the filamentarity are positive quantities. This choice does not affect our results, since $\mathcal{G} = 0$ for the great majority of the iso-surfaces analyzed in this study; however, if needed, one could use an available method[31] to include in the analysis the iso-surfaces with negative genus. Within the $\mathcal{G} = 0$ subset, $(\mathcal{P},\mathcal{F}) = (0,0)$ for a sphere,[31,32] $(\mathcal{P},\mathcal{F}) = (1,0)$ for a thin circular sheet,[31,32] $(\mathcal{P},\mathcal{F}) = (0,1)$ for an infinitely long tube,[31,32] and $(\mathcal{P},\mathcal{F}) = (1,1)$ for an infinitely long ribbon.[31,32] According to the visual shapes of the iso-surfaces extracted elsewhere,[31] the more complex (on average) is the structure of a surface, the larger is either $\mathcal{P}$ or $\mathcal{F}$.

To conduct the MF analysis, an iso-value for the iso-surfaces must be first selected. To this scope, we constructed the probability distribution function (PDF) $P(\eta)$ of the field (e.g., II_d or g) to be investigated, with η being the sample space for the field intensity. In assembling the PDF, we only considered the contributions from those regions of the flow where the local value of the field was above a threshold, which was taken to be a ten-thousandth of the global maximum of the field. Of note, for II_d, this choice implies that only contributions from vorticity-dominated regions (where II_d is positive; see below) are taken into account. The iso-value η_{iso} of the iso-surfaces to be extracted was then computed as

$$\int_{-\infty}^{\eta_{\text{iso}}} P(\eta)d\eta = P_{\text{iso}}, \tag{33}$$

with $P_{\text{iso}} = 0.9$. This choice guarantees the extraction of a statistically relevant number of structures for the different filter widths considered. Different iso-values, corresponding to values of P_{iso} ranging between 0.87 and 0.93, were also tested for completeness. Despite a variation in the size of the extracted structures, it was observed that their shape, spatial distribution, and morphology were only little affected by the choice of the threshold value, similarly to conclusions reached elsewhere.[31]

2. MF analysis of the second invariant of $\nabla\mathbf{u}$

The definition of II_d is

$$II_d = \frac{1}{2}\left[\frac{1}{2}\omega_i\omega_i - (S_{ij}S_{ij})\right], \tag{34}$$

where $\boldsymbol{\omega} = \nabla\times\mathbf{u}$ is the vorticity vector. According to the above definition, surfaces identified by large positive values of II_d are dominated by vorticity rather than strain. Iso-surfaces of II_d at t^*_{tr} are shown in Figs. 2(a), 2(c), and 2(e) for p60 and Figs. 3(a), 3(c), and 3(e) for p80. II_d was computed using either unfiltered (a) or the FC-DNS solution fields ((c) and (e); (c) corresponds to $\overline{\Delta} = 3\Delta x$, while (e) corresponds to $\overline{\Delta} = 6\Delta x$). When the solution fields are filtered, only the large-scale structures survive; consequently, a comparison between the filtered and unfiltered cases can be used to identify the structures having length scales smaller than $\overline{\Delta}$. For the iso-values considered here, most of the iso-surfaces have characteristic length scales that are smaller than the filter width since they

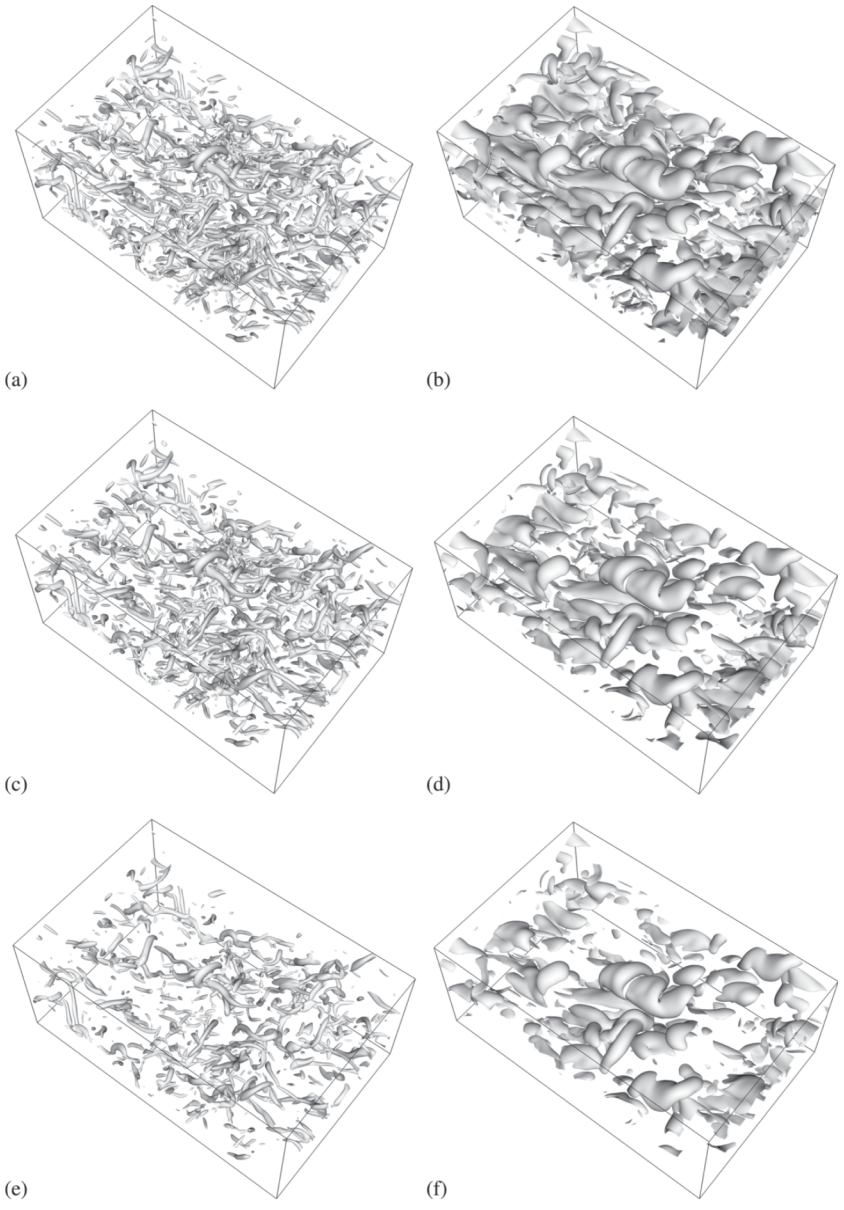

FIG. 2. Iso-surfaces of II_d (a), (c), (e) and g (b), (d), (f) for Re1000p60 at t^*_{tr}. DNS database (a), (b); filtered DNS database where $\overline{\Delta} = 3\Delta x$ (c), (d); and filtered DNS database where $\overline{\Delta} = 6\Delta x$ (e), (f).

disappear as the solution fields are filtered; in particular, the higher the value of $\overline{\Delta}$, the larger the number of iso-surfaces removed. This is clearly shown in both Fig. 2 for $p_0 = 60$ bar and Fig. 3 for $p_0 = 80$ bar. The value of p_0 seems to slightly affect the spatial distribution of the iso-surfaces, which appear to be less homogeneously distributed in the mixing layer for larger values of p_0; this may be a consequence of the increasing difficulty to entrain a denser fluid as p_0 is increased.

The scatter plots of $\mathcal{F}$ versus $\mathcal{P}$ for the II_d iso-surfaces are displayed in Figs. 4(a) and 4(b) for p60 and p80, respectively. Data are shown both for the DNS solutions and for $\overline{\Delta} = 3\Delta x$ or $\overline{\Delta} = 6\Delta x$. For p60 (Fig. 4(a)), the DNS database exhibits surfaces generally having greater $\mathcal{F}$ than $\mathcal{P}$ whereas for p80 (4(b)), the spread of $\mathcal{P}$ values slightly increases while that of $\mathcal{F}$ slightly decreases. This indicates a somewhat different morphology of the flow for $p_0 = 80$ bar due to the increased density at increasing p_0, making it more difficult to entrain and form filaments. Despite these differences, the surfaces are characterized by high $\mathcal{F}$ and low $\mathcal{P}$ values for both cases. Filtering removes the

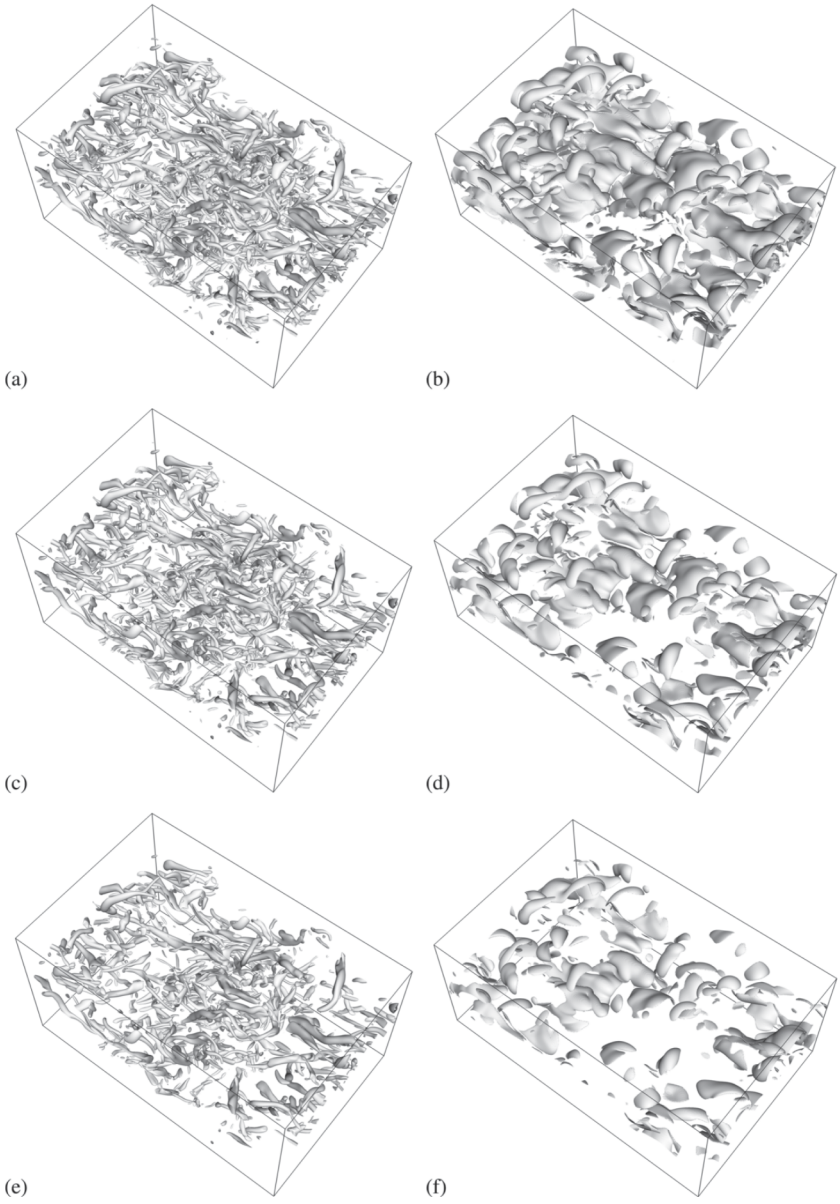

FIG. 3. Iso-surfaces of II_d (a), (c), (e) and g (b), (d), (f) for Re1000p80 at t^*_{tr}. DNS database (a), (b); filtered DNS database where $\overline{\Delta} = 3\Delta x$ (c), (d); and filtered DNS database where $\overline{\Delta} = 6\Delta x$ (e), (f).

surfaces with higher $\mathcal{P}$ while those with higher $\mathcal{F}$ are apparently better maintained. These results indicate that the LES flow fields should be characterized by structures of II_d that are rather more filamentary than planar in nature.

3. MF analysis of the dissipation

The general mathematical form of the irreversible entropy production rate has already been derived in the past.[19,29,37] Following previous notation,[7]

$$g = \underbrace{\frac{\mu}{T}\left(2S_{ij}S_{ij} - \tfrac{2}{3}S_{kk}S_{ll}\right)}_{g_{visc}} - \underbrace{\frac{q_j}{T^2}\frac{\partial T}{\partial x_j}}_{g_{heat}} - \underbrace{\sum_{\alpha=1}^{N}\frac{j_{\alpha j}}{m_\alpha}\frac{\partial}{\partial x_j}\left(\frac{\mu_\alpha}{T}\right)}_{g_{mass,flux}}, \tag{35}$$

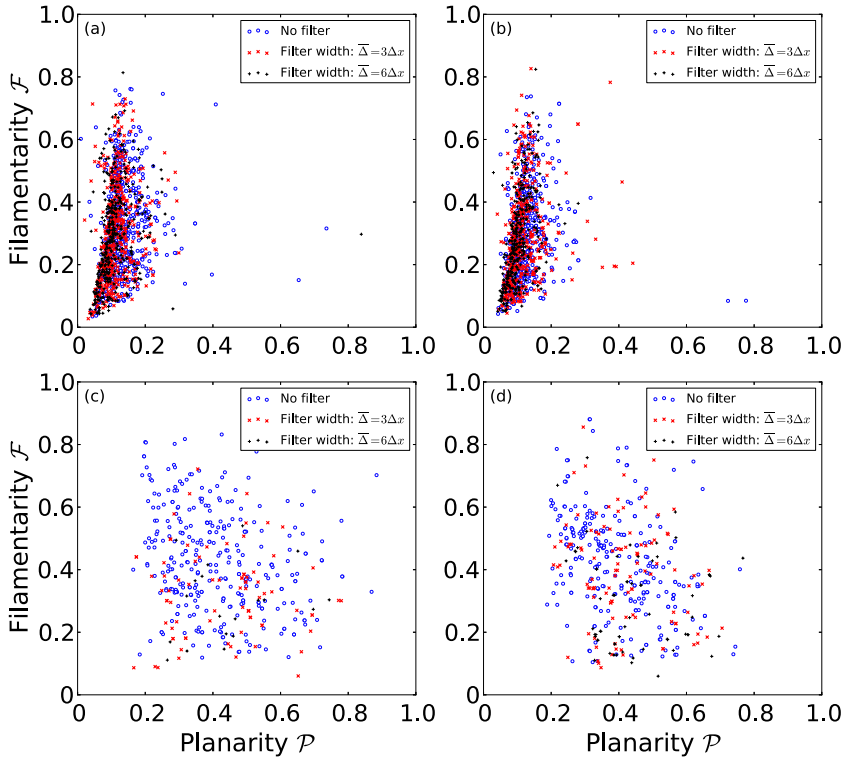

FIG. 4. Scatter plot of the filamentarity versus planarity for iso-surfaces of (a), (b) the second invariant of $\nabla\mathbf{u}$ and (c), (d) the dissipation, g, all at t^*_{tr}. (a), (c) p60 and (b), (d) p80 for the DNS database and the filtered database with either $\overline{\Delta}=3\Delta x$ or $\overline{\Delta}=6\Delta x$.

where $\mu_\alpha = h_\alpha - Ts_\alpha$ is the chemical potential of species α as defined in Sec. II A, with s_α being the partial molar entropy. Further manipulations of Eq. (35) lead to

$$g = \underbrace{\frac{\mu}{T}\left(2S_{ij}S_{ij} - \tfrac{2}{3}S_{kk}S_{ll}\right)}_{g_{visc}} + \underbrace{\lambda\frac{1}{T^2}\frac{\partial T}{\partial x_j}\frac{\partial T}{\partial x_j}}_{g_{temp}} + \underbrace{\frac{1}{2}\sum_{\beta=1}^{N}\sum_{\alpha=1}^{N}\frac{R_u}{(-\mathbb{D}_{\alpha\beta})}\frac{\rho}{m_\alpha Y_\beta}\Pi_{\alpha\beta j}\Pi_{\alpha\beta j}}_{g_{mass}} \tag{36}$$

where $((-\mathbb{D}_{\alpha\beta}m)/(Y_\alpha m_\beta))$ is a symmetric positive semi-definite matrix[38,39] and

$$\Pi_{\alpha\beta j} = -X_\beta\mathbb{D}_{\alpha\beta}\left[\left(\frac{m_\alpha}{m}\bar{\alpha}^b_{T,\beta} - \frac{m_\beta}{m}\bar{\alpha}^b_{T,\alpha}\right)\frac{1}{T}\frac{\partial T}{\partial x_j} + \frac{m_\alpha m_\beta}{mR_uT}\left(\frac{v_\alpha}{m_\alpha} - \frac{v_\beta}{m_\beta}\right)\frac{\partial p}{\partial x_j}\right]$$
$$- \sum_{\gamma=1}^{N-1}\left(\frac{m_\beta}{m_\gamma}\mathbb{D}_{\beta\alpha}\alpha_{D\alpha\gamma} - \frac{m_\alpha}{m_\gamma}\mathbb{D}_{\alpha\beta}\alpha_{D\beta\gamma}\right)\left[\frac{\partial Y_\gamma}{\partial x_j} - Y_\gamma\sum_{\delta=1}^{N-1}\left(\frac{m}{m_\delta} - \frac{m}{m_N}\right)\frac{\partial Y_\delta}{\partial x_j}\right]. \tag{37}$$

The g iso-surfaces at t^*_{tr} are presented in Figs. 2(b), 2(d), and 2(f) for p60 and Figs. 3(b), 3(d), and 3(f) for p80. Following the same procedure that was adopted for II_d, g was computed using both unfiltered (b) and the FC-DNS ((d) and (f)) solution fields. Visually, the g iso-surfaces look more extensive than the II_d ones; additionally, their spatial distribution appears to be less chaotic that the one exhibited by the iso-surfaces of II_d. As the p_0 value is increased, the iso-surfaces become more sparse (compare Figs. 2(b), 2(c), and 2(d) to Figs. 3(b), 3(c), and 3(d), respectively); this effect is again attributed to the increased difficulty in achieving mixing between two fluids as they become denser.

The scatter plots of $\mathcal{F}$ versus $\mathcal{P}$ for the g iso-surfaces are shown in Figs. 4(c) and 4(d) for p60 and p80, respectively. Analysis of the DNS solutions reveals that these iso-surfaces, although much reduced in number and sparse in distribution, usually have a more complex morphological

and geometrical aspect than the II_d ones; in fact, there are scarcely any low-complexity-structure iso-surfaces for g. Filtering the solution fields (i.e., removing the small scale structures from the DNS solutions) results in the removal of some of the high-complexity structures of g; however, for given value of $\overline{\Delta}$, the remaining large-scale structures still retain a higher morphological complexity than the equivalent ones for II_d. These results indicate that, in the LES solutions corresponding to the mixing layer information listed in Table II, the large-scale structures of g should have, statistically, higher values of planarity and filamentarity than those of II_d. Since in these transitional flows g is primarily related to thermodynamic effects,[7] this MF analysis is an indicator that representing the effects of unconventional SGS models may be necessary to obtain high-fidelity LES.

B. *A priori* analysis

Because the interest is in reproducing in LES the physics of the DNS database, we first determine the importance of each phenomenon represented in the conservation equations by assessing the activity of each term appearing in Eqs. (3) and (4). That is, we do not compare each of the terms with the leading-order term which is $O(10)$-$O(10^2)$ larger than other terms, as shown below; if we did so, for the chosen values of $\overline{\Delta}$, there would be no rationale to retain a single of the SGS terms. What we are comparing is a resolved term and its SGS contribution in order to evaluate if the latter is a significant percentage of the former, in which case modeling of the SGS term is necessary to accurately portray the physics embedded in that term. Clearly, if both a resolved and unresolved terms have contributions negligible with respect to the leading order term, modeling of that SGS term is unnecessary. In performing this analysis, the unclosed terms not associated with the conventional SGS fluxes are rewritten according to Eq. (27). Since in the supercritical-p realm, the ability of the typical SGS models (Smagorinsky model, the gradient model, and the scale-similarity model) to reproduce the conventional SGS fluxes has already been assessed,[12] the results described below indicate that we should focus on $\overline{p(\phi)}$, $\overline{q_j(\phi)}$, and $\overline{J_{\alpha j}(\phi)}$. This assessment is first made in Sec. IV B 1 from the standpoint of domain averages. Models for the unconventional SGS terms are proposed and subsequently assessed on a planar average basis in Sec. IV B 2.

1. Activity of terms in the LES equations

The activity of terms appearing in Eqs. (3) and (4) is given in Tables III-X in terms of their root mean square σ_{rms}. The root mean square of a spatial field f is defined as the square root of its variance f'^2,

$$f'^2 = \left\langle\left\langle (f - \langle\langle f\rangle\rangle)^2\right\rangle\right\rangle = \langle\langle f^2\rangle\rangle - \langle\langle f\rangle\rangle^2, \tag{38}$$

where $\langle\langle\rangle\rangle$ denotes averaging over the entire computational domain. Although the flow evolution in DNS will not be the same as in LES, it seems reasonable to assume that, in LES, unclosed terms

TABLE III. Activity (rms) of terms at t_{tr}^* in the first component of the LES momentum equation. Units are 10^6 N m^{-3}.

	$\overline{\Delta} = 3\Delta x$		$\overline{\Delta} = 6\Delta x$	
x_1-momentum	p60	p80	p60	p80
$\frac{\partial}{\partial x_j}(\overline{\rho}\widetilde{u_1}\widetilde{u_j})$	24.29	40.88	22.13	37.11
$\frac{\partial}{\partial x_1}\left[p(\overline{\phi})\right]$	7.953	11.63	9.359	13.40
$\frac{\partial}{\partial x_j}\left[\sigma_{1j}(\overline{\phi})\right]$	0.741	1.276	0.612	1.068
$\frac{\partial}{\partial x_j}(\overline{\rho}\tau_{1j})$	0.488	0.694	0.728	1.051
$\frac{\partial}{\partial x_1}[\Delta(\overline{p})]$	6.191	8.608	7.957	10.95
$\frac{\partial}{\partial x_j}\left[\Delta\overline{\sigma_{1j}(\phi)}\right]$	0.142	0.265	0.155	0.285
	$\Delta(\bar{f}) \equiv \overline{f(\phi)} - f(\bar{\phi})$			

TABLE IV. Activity (rms) of terms at t^*_{tr} in the second component of the LES momentum equation. Units are 10^6 N m^{-3}.

	$\overline{\Delta} = 3\Delta x$		$\overline{\Delta} = 6\Delta x$	
x_2-momentum	p60	p80	p60	p80
$\frac{\partial}{\partial x_j}(\overline{\rho}\widetilde{u_2}\widetilde{u_j})$	11.09	18.65	10.22	17.33
$\frac{\partial}{\partial x_2}\left[p(\overline{\phi})\right]$	10.47	15.25	12.86	18.28
$\frac{\partial}{\partial x_j}\left[\sigma_{2j}(\overline{\phi})\right]$	0.646	1.128	0.533	0.947
$\frac{\partial}{\partial x_j}(\overline{\rho}\tau_{2j})$	0.422	0.604	0.637	0.931
$\frac{\partial}{\partial x_2}[\Delta(\overline{p})]$	9.279	13.22	11.94	16.73
$\frac{\partial}{\partial x_j}\left[\Delta\overline{\sigma_{2j}(\phi)}\right]$	0.095	0.187	0.103	0.202
	$\Delta(\bar{f}) \equiv \overline{f(\phi)} - f(\bar{\phi})$			

with large activities may need more accurate modeling than terms with low activities. Results are given in the tables for both simulations in the DNS database at their corresponding transitional time t^*_{tr}, each for $\overline{\Delta} = 3\Delta x$ and $\overline{\Delta} = 6\Delta x$.

For the momentum equation (Tables III-V), the terms with the largest activity correspond to the inviscid resolved terms, $\nabla \cdot (\overline{\rho}\,\widetilde{\mathbf{u}}\,\widetilde{\mathbf{u}})$ and $\nabla p(\overline{\phi})$, and to the unconventional SGS pressure term, $\nabla[\overline{p(\phi)} - p(\overline{\phi})]$. The activity of the remaining terms is approximately one to two orders of magnitude smaller than that of the leading terms. Under supercritical-p conditions, the pressure is a strongly non-linear function of the flow variables and it is thus expected that, with increasing $\overline{\Delta}$, the difference between $\overline{p(\phi)}$ and $p(\overline{\phi})$ should also increase. This is indeed confirmed by the fact that, with increasing $\overline{\Delta}$, the activity of $\nabla[\overline{p(\phi)} - p(\overline{\phi})]$ increases at a higher rate than that of $\nabla p(\overline{\phi})$, indicating that an accurate model for the unconventional SGS pressure term may be important for LES of supercritical-p flows. Taking Table III as an example, for Run p60, the results show that not only does $\frac{\partial}{\partial x_j}(\overline{\rho}\tau_{1j})$ represent 66% of $\frac{\partial}{\partial x_j}\left[\sigma_{1j}(\overline{\phi})\right]$ for $\overline{\Delta} = 3\Delta x$ and 119% for $\overline{\Delta} = 6\Delta x$ but also $\frac{\partial}{\partial x_1}[\Delta(\overline{p})]$ represents 78% of $\frac{\partial}{\partial x_1}\left[p(\overline{\phi})\right]$ for $\overline{\Delta} = 3\Delta x$ and 85% for $\overline{\Delta} = 6\Delta x$. The $\overline{\rho}\tau_{1j}$ term is of dissipative nature, but the $\Delta(\overline{p})$ term is not so, showing that both values of $\overline{\Delta}$ are in the coarse-grid LES regime. Of note, at $\overline{\Delta} = 6\Delta x$, the SGS viscous stress contribution is larger than that of the resolved stresses, indicating the meaningfulness of both the database and the chosen $\overline{\Delta}$.

For the energy equation (Table VI), the convective term has the largest activity, followed by a group of terms with similar magnitude which comprises the resolved pressure work, the conventional SGS flux, the resolved heat flux, and the unconventional SGS terms due to pressure work, $\nabla \cdot [(\overline{p(\phi)} - p(\overline{\phi}))\widetilde{\mathbf{u}}]$, and the heat flux, $\nabla \cdot [\overline{\mathbf{q}(\phi)} - \mathbf{q}(\overline{\phi})]$. The ratio between these two categories of terms is of approximately two order of magnitudes, independently of the $\overline{\Delta}$ value considered.

TABLE V. Activity (rms) of terms at t^*_{tr} in the third component of the LES momentum equation. Units are 10^6 N m^{-3}.

	$\overline{\Delta} = 3\Delta x$		$\overline{\Delta} = 6\Delta x$	
x_3-momentum	p60	p80	p60	p80
$\frac{\partial}{\partial x_j}(\overline{\rho}\widetilde{u_3}\widetilde{u_j})$	10.58	17.46	9.700	16.12
$\frac{\partial}{\partial x_3}\left[p(\overline{\phi})\right]$	8.675	12.81	10.50	15.13
$\frac{\partial}{\partial x_j}\left[\sigma_{3j}(\overline{\phi})\right]$	0.678	1.175	0.560	0.989
$\frac{\partial}{\partial x_j}(\overline{\rho}\tau_{3j})$	0.448	0.626	0.678	0.963
$\frac{\partial}{\partial x_3}[\Delta(\overline{p})]$	7.433	10.67	9.557	13.47
$\frac{\partial}{\partial x_j}\left[\Delta\overline{\sigma_{3j}(\phi)}\right]$	0.102	0.196	0.101	0.210
	$\Delta(\bar{f}) \equiv \overline{f(\phi)} - f(\bar{\phi})$			

TABLE VI. Activity (rms) of terms at t_{tr}^* in the LES energy equation. Units are 10^9 J m^{-3} s^{-1}.

	$\overline{\Delta} = 3\Delta x$		$\overline{\Delta} = 6\Delta x$	
Energy	p60	p80	p60	p80
$\frac{\partial}{\partial x_j}(\overline{\rho}\widetilde{e_t}\widetilde{u_j})$	449.1	674.9	406.5	606.3
$\frac{\partial}{\partial x_j}\left[p(\overline{\phi})\widetilde{u_j}\right]$	2.473	3.881	2.613	4.118
$\frac{\partial}{\partial x_j}\left[q_j(\overline{\phi})\right]$	13.73	21.40	11.11	17.38
$\frac{\partial}{\partial x_j}\left[\sigma_{ij}(\overline{\phi})\widetilde{u_i}\right]$	0.070	0.132	0.059	0.111
$\frac{\partial}{\partial x_j}(\overline{\rho}\zeta_j)$	7.254	11.34	10.23	16.15
$\frac{\partial}{\partial x_j}(\overline{\rho}\tau_{ij}\widetilde{u_i})$	0.042	0.074	0.060	0.100
$\frac{\partial}{\partial x_j}[\overline{\rho}(\kappa_j - \tau_{ij}\widetilde{u_i})]$	0.017	0.040	0.020	0.044
$\frac{\partial}{\partial x_j}[\Delta(\overline{p})\widetilde{u_j}]$	0.560	0.839	0.768	1.148
$\frac{\partial}{\partial x_j}[\Delta(\overline{q_j})]$	3.436	5.775	3.649	6.098
$\frac{\partial}{\partial x_j}[\Delta(\overline{\sigma_{ij}u_i})]$	0.017	0.032	0.020	0.036
$\kappa_j = \vartheta(\widetilde{e}_K, \widetilde{u}_j), \Delta(\bar{f}) \equiv \overline{f(\phi)} - f(\bar{\phi})$				

Taking as an example Run p60 for $\overline{\Delta} = 6\Delta x$, $\nabla \cdot [\overline{\rho}\boldsymbol{\tau}\widetilde{\mathbf{u}}]$ represents 102% of the resolved term $\nabla \cdot [\overline{\rho}\boldsymbol{\sigma}(\overline{\phi})\widetilde{\mathbf{u}}]$, $\nabla \cdot [\overline{\mathbf{q}(\phi)} - \mathbf{q}(\overline{\phi})]$ represents 33% of the resolved term $\nabla \cdot \mathbf{q}(\overline{\phi})$, and $\nabla \cdot [(\overline{p(\phi)} - p(\overline{\phi}))\widetilde{\mathbf{u}}]$ represents 29% of the resolved term $\nabla \cdot [p(\overline{\phi})\widetilde{\mathbf{u}}]$. Since we know that the resolved terms must be kept in the LES equations, this numerical evaluation indicates that the unconventional SGS terms $\nabla \cdot [\overline{\mathbf{q}(\phi)} - \mathbf{q}(\overline{\phi})]$ and $\nabla \cdot [(\overline{p(\phi)} - p(\overline{\phi}))\widetilde{\mathbf{u}}]$ must be kept as well since they both represent a significant part of the corresponding resolved term. The term $\nabla \cdot [(\overline{p(\phi)} - p(\overline{\phi}))\widetilde{\mathbf{u}}]$ was not significant with respect to $\nabla \cdot [p(\overline{\phi})\widetilde{\mathbf{u}}]$ in our previous study of binary-species mixing under supercritical-p conditions;[12] its increased importance here is attributed to the larger $\mathrm{Re}_{m,tr}$ values reached in the mixing layers. The remaining terms in the energy equation have negligible activity.

Finally, in examining the activity of terms for the species LES equations, we distinguish between the equations for the major species, n-C_7H_{16} and O_2 (Tables VII and VIII), and those for the minor species, H_2O and CO_2 (Tables IX and X). Although for each species the convective term is dominant, the activity of the unconventional SGS term due to the species molecular flux, $\nabla \cdot [\overline{\mathbf{J}_\alpha(\phi)} - \mathbf{J}_\alpha(\overline{\phi})]$, is significant (i.e., of the order of 40%) with respect to its resolved counterpart $\nabla \cdot \mathbf{J}_\alpha(\overline{\phi})$ for the major species, while this is not the case for the minor species. This fact is attributed to the much smaller fluxes of H_2O and CO_2 (having mass fractions which are initially uniform in the entire domain) relative to those of n-C_7H_{16} and O_2. For n-C_7H_{16} (Table VII), the results for Run p60 and $\overline{\Delta} = 6\Delta x$ indicate that conventional SGS effects are important since $\nabla \cdot (\overline{\rho}\boldsymbol{\eta})$ represents 139% of the resolved term $\nabla \cdot \mathbf{J}_\alpha(\overline{\phi})$; but unconventional SGS terms are also important since $\nabla \cdot [\overline{\mathbf{J}_\alpha(\phi)} - \mathbf{J}_\alpha(\overline{\phi})]$ represents 37% of $\nabla \cdot \mathbf{J}_\alpha(\overline{\phi})$. For H_2O (Table IX), equivalent results for Run p60 and $\overline{\Delta} = 6\Delta x$ show that $\nabla \cdot (\overline{\rho}\boldsymbol{\eta})$ represents 100% of $\nabla \cdot \mathbf{J}_\alpha(\overline{\phi})$ and $\nabla \cdot [\overline{\mathbf{J}_\alpha(\phi)} - \mathbf{J}_\alpha(\overline{\phi})]$ represents

TABLE VII. Activity (rms) of terms at t_{tr}^* in the LES conservation equation for n-heptane. Units are 10^4 kg s^{-1} m^{-3}.

	$\overline{\Delta} = 3\Delta x$		$\overline{\Delta} = 6\Delta x$	
C_7H_{16}	p60	p80	p60	p80
$\frac{\partial}{\partial x_j}\left(\overline{\rho}\widetilde{Y}\widetilde{u_j}\right)$	27.63	41.39	24.78	36.79
$\frac{\partial}{\partial x_j}\left[J_j(\overline{\phi})\right]$	0.584	0.876	0.444	0.669
$\frac{\partial}{\partial x_j}(\overline{\rho}\eta_j)$	0.457	0.727	0.617	0.981
$\frac{\partial}{\partial x_j}\left[\Delta(\overline{J_j(\phi)})\right]$	0.166	0.278	0.165	0.273
$\Delta(\bar{f}) \equiv \overline{f(\phi)} - f(\bar{\phi})$				

TABLE VIII. Activity (rms) of terms at t^*_{tr} in the LES conservation equation for oxygen. Units are 10^4 kg s^{-1} m^{-3}.

	$\overline{\Delta}=3\Delta x$		$\overline{\Delta}=6\Delta x$	
O_2	p60	p80	p60	p80
$\frac{\partial}{\partial x_j}\left(\overline{\rho}\widetilde{Y}\widetilde{u_j}\right)$	0.682	0.977	0.621	0.889
$\frac{\partial}{\partial x_j}\left[J_j(\overline{\phi})\right]$	0.124	0.187	0.096	0.145
$\frac{\partial}{\partial x_j}(\overline{\rho}\eta_j)$	0.089	0.142	0.122	0.194
$\frac{\partial}{\partial x_j}\left[\Delta(\overline{J_j(\phi)})\right]$	0.033	0.056	0.033	0.055
	$\Delta(\bar{f})\equiv\overline{f(\phi)}-f(\bar{\phi})$			

14% of $\nabla\cdot\mathbf{J}_\alpha(\overline{\phi})$, thus making the unconventional SGS term of marginal importance. Compared to our previous binary-species study,[12] the increased importance of $\nabla\cdot[\overline{\mathbf{J}_\alpha(\phi)}-\mathbf{J}_\alpha(\overline{\phi})]$ with respect to $\nabla\cdot\mathbf{J}_\alpha(\overline{\phi})$ for n-C_7H_{16} and for O_2 is attributed to the larger values of $\mathrm{Re}_{m,tr}$ obtained in the present DNS database with respect to the binary-species simulations[8] used in that analysis.[12] For the present conditions, the activity of $\nabla\cdot(\overline{\rho}\boldsymbol{\eta})$ is comparable to (exceeds) that of $\nabla\cdot\mathbf{J}_\alpha(\overline{\phi})$ for all species at $\overline{\Delta}=3\Delta x$ ($\overline{\Delta}=6\Delta x$).

2. Modeling of $\overline{p(\boldsymbol{\phi})}$, $\overline{\mathbf{q}(\boldsymbol{\phi})}$, and $\overline{\mathbf{J}_\alpha(\boldsymbol{\phi})}$

The analysis of the activity of terms in the conservation equations has shown that some of the unconventional SGS terms are not negligible. These terms correspond to the SGS pressure term in the momentum equation, $\nabla[\overline{p(\phi)}-p(\overline{\phi})]$, to the SGS species fluxes in the species equations, $\nabla\cdot[\overline{\mathbf{J}_\alpha(\phi)}-\mathbf{J}_\alpha(\overline{\phi})]$, and to the SGS heat flux and the SGS pressure work in the energy equation, $\nabla\cdot[\overline{\mathbf{q}(\phi)}-\mathbf{q}(\overline{\phi})]$ and $\nabla[\overline{(p(\phi)-p(\overline{\phi}))\widetilde{\mathbf{u}}}]$. The fact that their contribution is important implies that closures for $\overline{p(\phi)}$, $\overline{\mathbf{q}(\phi)}$, and $\overline{\mathbf{J}_\alpha(\phi)}$ based on the classical LES assumptions given by Eq. (25) may not be appropriate for LES of supercritical-p flows.

Improved models for $\overline{p(\phi)}$, $\overline{\mathbf{q}(\phi)}$, and $\overline{\mathbf{J}_\alpha(\phi)}$ can be obtained by extending the scale similarity model[40] to functions of the conservative fields ϕ. Following this approach, we define a test-filtering operation $\widehat{()}$ and $\widehat{\Delta}$ which is the filter width associated with the test filter. For the grid-level and test-level SGS species fluxes are defined as

$$\vartheta(\phi)=\overline{p(\phi)}-p(\overline{\phi}), \tag{39}$$

$$\mathcal{T}(\phi)=\vartheta(\overline{\phi})=\widehat{\overline{p(\phi)}}-p(\widehat{\overline{\phi}}). \tag{40}$$

The test-level resolved scalar can be expressed through the following Germano identity:[41]

$$L_p=\mathcal{T}-\widehat{\vartheta}=\widehat{p(\overline{\phi})}-p(\widehat{\overline{\phi}}), \tag{41}$$

TABLE IX. Activity (rms) of terms at t^*_{tr} in the LES conservation equation for water. Units are 10^4 kg s^{-1} m^{-3}.

	$\overline{\Delta}=3\Delta x$		$\overline{\Delta}=6\Delta x$	
H_2O	p60	p80	p60	p80
$\frac{\partial}{\partial x_j}\left(\overline{\rho}\widetilde{Y}\widetilde{u_j}\right)$	0.175	0.268	0.164	0.250
$\frac{\partial}{\partial x_j}\left[J_j(\overline{\phi})\right]$	0.008	0.013	0.007	0.010
$\frac{\partial}{\partial x_j}(\overline{\rho}\eta_j)$	0.006	0.010	0.007	0.011
$\frac{\partial}{\partial x_j}\left[\Delta(\overline{J_j(\phi)})\right]$	0.001	0.002	0.001	0.002
	$\Delta(\bar{f})\equiv\overline{f(\phi)}-f(\bar{\phi})$			

TABLE X. Activity (rms) of terms at t^*_{tr} in the LES conservation equation for carbon dioxide. Units are 10^4 kg s^{-1} m^{-3}.

	$\overline{\Delta} = 3\Delta x$		$\overline{\Delta} = 6\Delta x$	
CO_2	p60	p80	p60	p80
$\frac{\partial}{\partial x_j}\left(\overline{\rho}\widetilde{Y}\widetilde{u_j}\right)$	0.612	0.918	0.576	0.860
$\frac{\partial}{\partial x_j}\left[J_j(\overline{\phi})\right]$	0.029	0.049	0.023	0.039
$\frac{\partial}{\partial x_j}\left(\overline{\rho}\eta_j\right)$	0.024	0.041	0.027	0.047
$\frac{\partial}{\partial x_j}\left[\Delta(\overline{J_j(\phi)})\right]$	0.005	0.011	0.004	0.009
	$\Delta(\bar{f}) \equiv \overline{f(\phi)} - f(\bar{\phi})$			

which is used in the following to evaluate the scale-similarity coefficient. Within the context of scale-similarity models, the grid-level and test-level SGS quantities can be modeled as

$$\vartheta(\phi) = C'\left[\overline{p(\overline{\phi})} - p(\overline{\overline{\phi}})\right], \tag{42}$$

$$\mathcal{T}(\phi) = C''\left[\widehat{\overline{p(\widehat{\overline{\phi}})}} - p(\widehat{\overline{\overline{\phi}}})\right]. \tag{43}$$

Assuming $C_p = C' = C''$, the Germano identity can be rewritten as

$$L_p = C_p \cdot M_p, \quad M_p = \left[\widehat{\overline{p(\widehat{\overline{\phi}})}} - p(\widehat{\overline{\overline{\phi}}})\right] - \left[\widehat{\overline{p(\overline{\phi})}} - \widehat{p(\overline{\overline{\phi}})}\right]. \tag{44}$$

Following Lilly,[42] the value of the coefficient C_p that minimize errors can be computed using a least-square method, resulting in

$$C_p = \frac{\langle M_p L_p \rangle}{\langle M_p M_p \rangle}. \tag{45}$$

For the fluxes, a similar development leads to

$$L_{j,\mathbf{J}_\alpha} = C_{\mathbf{J}_\alpha} \cdot M_{j,\mathbf{J}_\alpha}, \quad M_{j,\mathbf{J}_\alpha} = \left[\widehat{\overline{J_{\alpha,j}(\widehat{\overline{\phi}})}} - J_{\alpha,j}(\widehat{\overline{\overline{\phi}}})\right] - \left[\widehat{\overline{J_{\alpha,j}(\overline{\phi})}} - \widehat{J_{\alpha,j}(\overline{\overline{\phi}})}\right], \tag{46}$$

$$L_{j,\mathbf{q}} = C_{\mathbf{q}} \cdot M_{j,\mathbf{q}}, \quad M_{j,\mathbf{q}} = \left[\widehat{\overline{q_j(\widehat{\overline{\phi}})}} - q_j(\widehat{\overline{\overline{\phi}}})\right] - \left[\widehat{\overline{q_j(\overline{\phi})}} - \widehat{q_j(\overline{\overline{\phi}})}\right], \tag{47}$$

and the coefficients minimizing these errors are computed as

$$C_{\mathbf{J}_\alpha} = \frac{\langle M_{j,\mathbf{J}_\alpha} L_{j,\mathbf{J}_\alpha} \rangle}{\langle M_{j,\mathbf{J}_\alpha} M_{j,\mathbf{J}_\alpha} \rangle} \quad C_{\mathbf{q}} = \frac{\langle M_{j,\mathbf{q}} L_{j,\mathbf{q}} \rangle}{\langle M_{j,\mathbf{q}} M_{j,\mathbf{q}} \rangle}. \tag{48}$$

These models are labelled "improved LES assumptions" (ILAs) to clearly distinguish them from the SLA given by Eq. (25). In all calculations below, $\widehat{\Delta} = 2\overline{\Delta}$.

Illustrated in Fig. 5 are the coefficients computed according to Eqs. (45) and (48). Inside the mixing layer, C_p and $C_{\mathbf{q}}$ are both bounded in $[0.7, 2.2]$ while $C_{\mathbf{J}_\alpha} \in [0.5, 3]$. This shows that in the region of activity, the coefficients are positive and vary within a small range, thereby showing that they are well-conditioned and boding well for stable LES. At larger p_0, the coefficients vary in a narrower range than at smaller p_0, indicating increased LES stability, which is an important attribute. Outside of the mixing layer, the coefficients vary widely but during a LES computation they will be multiplied by very small values because $M_p, M_{j,\mathbf{J}_\alpha}$, and $M_{j,\mathbf{q}}$ are there indeed very small, and thus the stability of the LES will not be jeopardized.

The models given by the ILA are assessed here against those given by the SLA. To this scope, the DNS data were used to compute the homogeneous-plane rms of the difference between the

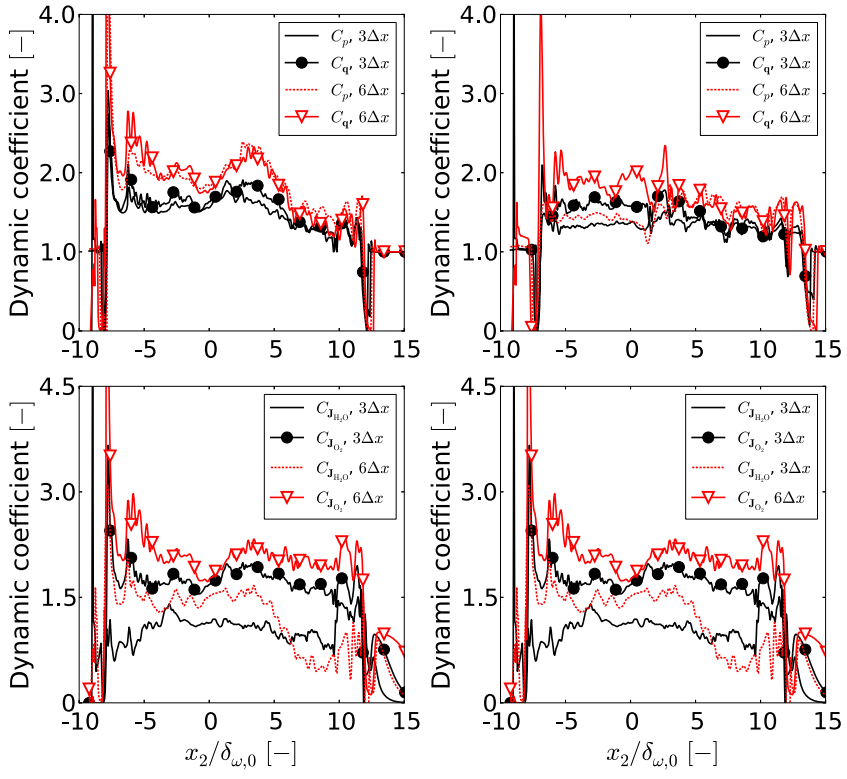

FIG. 5. Coefficients computed according to Eq. (45) for the pressure and Eq. (48) for the fluxes. Left column: results for p60. Right column: results for p80.

following exact terms, $\nabla\overline{p(\phi)}$, $\nabla(\overline{p(\phi)\widetilde{\mathbf{u}}})$, $\nabla\cdot\overline{\mathbf{J}_\alpha(\phi)}$, and $\nabla\cdot\overline{\mathbf{q}(\phi)}$, and their modeled counterparts, $\nabla\overline{p(\phi)}_{\mathrm{mod}}$, $\nabla\cdot(\overline{p(\phi)}_{\mathrm{mod}}\widetilde{\mathbf{u}})$, $\nabla\cdot\overline{\mathbf{J}_\alpha(\phi)}_{\mathrm{mod}}$, and $\nabla\cdot\overline{\mathbf{q}(\phi)}_{\mathrm{mod}}$, where $\overline{p(\phi)}_{\mathrm{mod}}$, $\overline{\mathbf{q}(\phi)}_{\mathrm{mod}}$, and $\overline{\mathbf{J}_\alpha(\phi)}_{\mathrm{mod}}$ are evaluated using either Eq. (25) or the following models:

$$\overline{p(\phi)} = p(\overline{\phi}) + C_p\cdot\left(\overline{p(\overline{\phi})} - p(\overline{\overline{\phi}})\right), \tag{49}$$

$$\overline{\mathbf{q}(\phi)} = \mathbf{q}(\overline{\phi}) + C_{\mathbf{q}}\cdot\left(\overline{\mathbf{q}(\overline{\phi})} - \mathbf{q}(\overline{\overline{\phi}})\right), \tag{50}$$

$$\overline{\mathbf{J}_\alpha(\phi)} = \mathbf{J}_\alpha(\overline{\phi}) + C_{\mathbf{J}_\alpha}\cdot\left(\overline{\mathbf{J}_\alpha(\overline{\phi})} - \mathbf{J}_\alpha(\overline{\overline{\phi}})\right). \tag{51}$$

The better a model is, the closer the rms is to zero. The findings are shown in Fig. 6 for $(\nabla\overline{p(\phi)} - \nabla\overline{p(\phi)}_{\mathrm{mod}})$, Fig. 7 for $(\nabla\cdot(\overline{p(\phi)\widetilde{\mathbf{u}}}) - \nabla\cdot(\overline{p(\phi)}_{\mathrm{mod}}\widetilde{\mathbf{u}}))$, Fig. 8 for $(\nabla\cdot\overline{\mathbf{J}_\alpha(\phi)} - \nabla\cdot\overline{\mathbf{J}_\alpha(\phi)}_{\mathrm{mod}})$ (the species considered for the analysis being H_2O and n-C_7H_{16}), and Fig. 9 for $(\nabla\cdot\overline{\mathbf{q}(\phi)} - \nabla\cdot\overline{\mathbf{q}(\phi)}_{\mathrm{mod}})$, all for $\overline{\Delta} = 3\Delta x$ and $\overline{\Delta} = 6\Delta x$. Results obtained for the fluxes of CO_2 and O_2 (not shown) are similar to those for the fluxes of H_2O and n-C_7H_{16}, respectively. All these models operate in the coarse-grid LES regime and their goal is to minimize the rms.

Figure 6 shows that the rms of $(\nabla\overline{p(\phi)} - \nabla\overline{p(\phi)}_{\mathrm{mod}})$ is larger in the upper part of the mixing layer and increases with increasing p_0 and $\overline{\Delta}$. These effects are direct consequences of the non-linear nature of the PR EOS; an increase in either p_0 or $\overline{\Delta}$ is expected to result in a larger difference between ϕ and $\overline{\phi}$ and thus in a higher difficulty in modeling $\overline{p(\phi)}$ as a combination of terms where p is evaluated in terms of $\overline{\phi}$; the range of the values on the axis confirms this interpretation. For p60, a doubling of $\overline{\Delta}$ induces a corresponding rms increase by approximately a factor of 2; however, for p80, the increase is only by a factor of 1/3. At $\overline{\Delta} = 3\Delta x$, an increase by a third in p_0 results in a nearly doubling of the rms, whereas at $\overline{\Delta} = 6\Delta x$, the rms increase is only approximately 1/3.

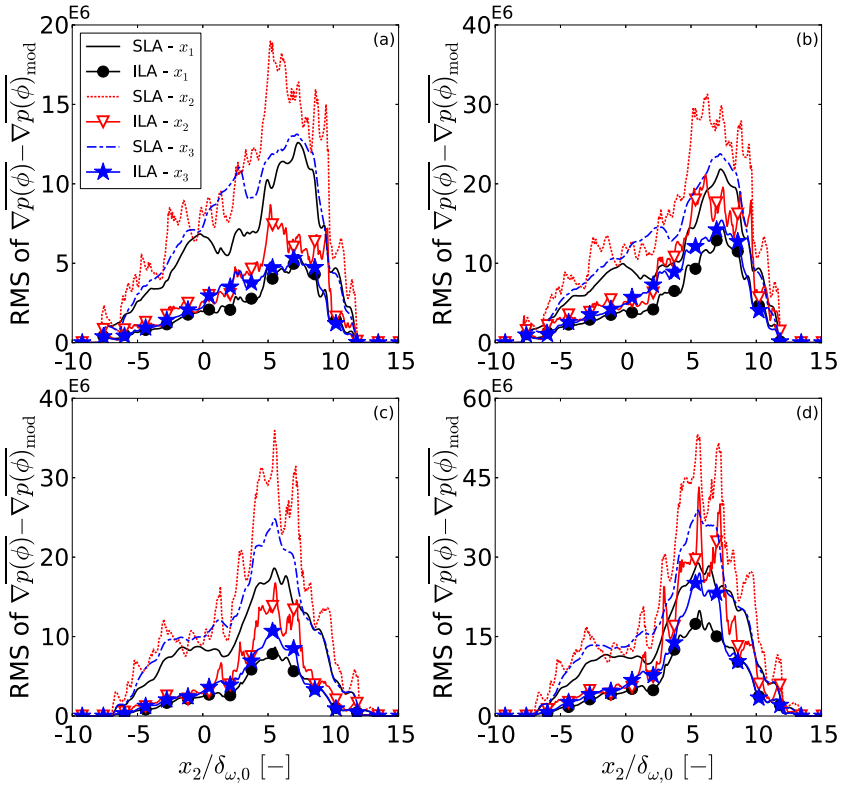

FIG. 6. The x_2-rms of the difference between exact and modeled values for the pressure-gradient SGS term for (a), (c) $\bar{\Delta} = 3\Delta x$ and (b), (d) $\bar{\Delta} = 6\Delta x$. (a), (b) p60 and (c), (d) p80, all at t^*_{tr}. The subscript *mod* labels the value computed using the model. "SLA" denotes the standard LES assumption and "ILA" labels the improved LES assumption. Units are in N m^{-3}.

Although the number of DNS realizations and the number of $\overline{\Delta}$ values are not large enough for a definite conclusion, it appears that at larger p_0 the rms does not increase proportionally with $\overline{\Delta}$, and that at larger $\overline{\Delta}$ the rms may increase proportionally with p_0. Previous studies[7] have shown that the largest difference between ϕ and $\overline{\phi}$ is localized to certain regions of the mixing layer;

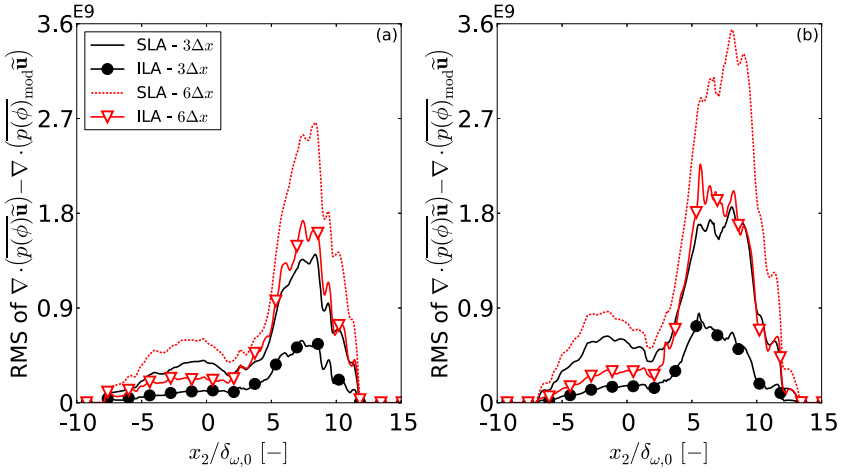

FIG. 7. The x_2-rms of the difference between exact and modeled values for the pressure-work SGS term for $\bar{\Delta} = 3\Delta x$ and $\bar{\Delta} = 6\Delta x$. (a) p60 and (b) p80, all at t^*_{tr}. The subscript *mod* labels the value computed using the model. "SLA" denotes the standard LES assumption and "ILA" labels the improved LES assumption. Units are J m^{-3} s^{-1}.

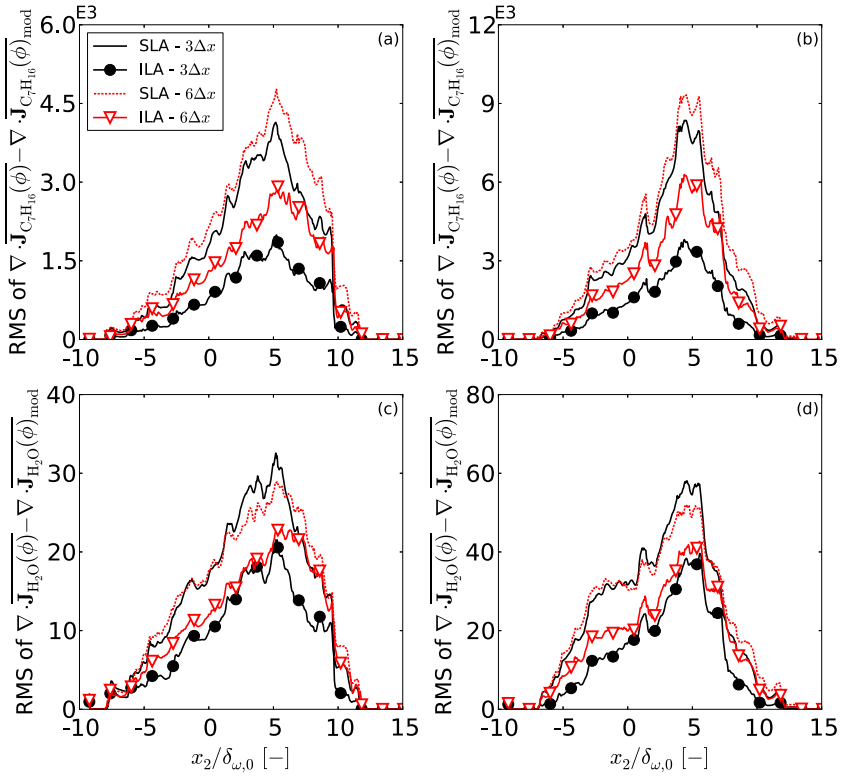

FIG. 8. The x_2-rms of the difference between the divergence of the filtered exact species-mass flux and the corresponding model for it. (a), (b) C_7H_{16} and (c), (d) H_2O. (a), (c) p60 and (b), (d) p80, all at t^*_{tr}. The subscript *mod* labels the value computed using the model. "SLA" denotes the standard LES assumption and "ILA" labels the improved LES assumption. Units are kg s^{-1} m^{-3}.

for example, a larger p_0 is responsible for an increasing difficulty in achieving good mixing between the upper and lower streams, resulting in the local formation of strong gradients of density, temperature, and species mass fractions. At $\overline{\Delta} = 3\Delta x$ and in the region of most activity, the ILA model for $\overline{p(\phi)}$ leads to a reduction in the modeling error by approximately 70% compared to

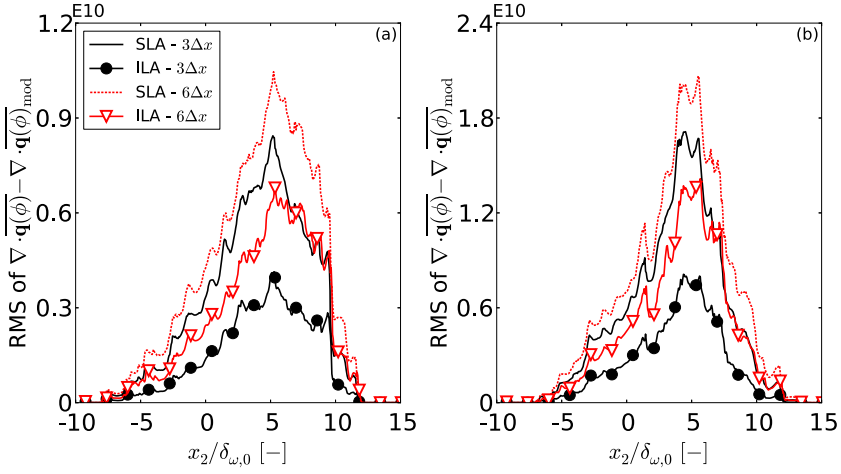

FIG. 9. The x_2-rms of the difference between the divergence of the filtered exact heat flux and the corresponding model for it. (a) p60 and (b) p80, all at t^*_{tr}. The subscript *mod* labels the value computed using the model. "SLA" denotes the standard LES assumption and "ILA" labels the improved LES assumption. Units are J m^{-3} s^{-1}.

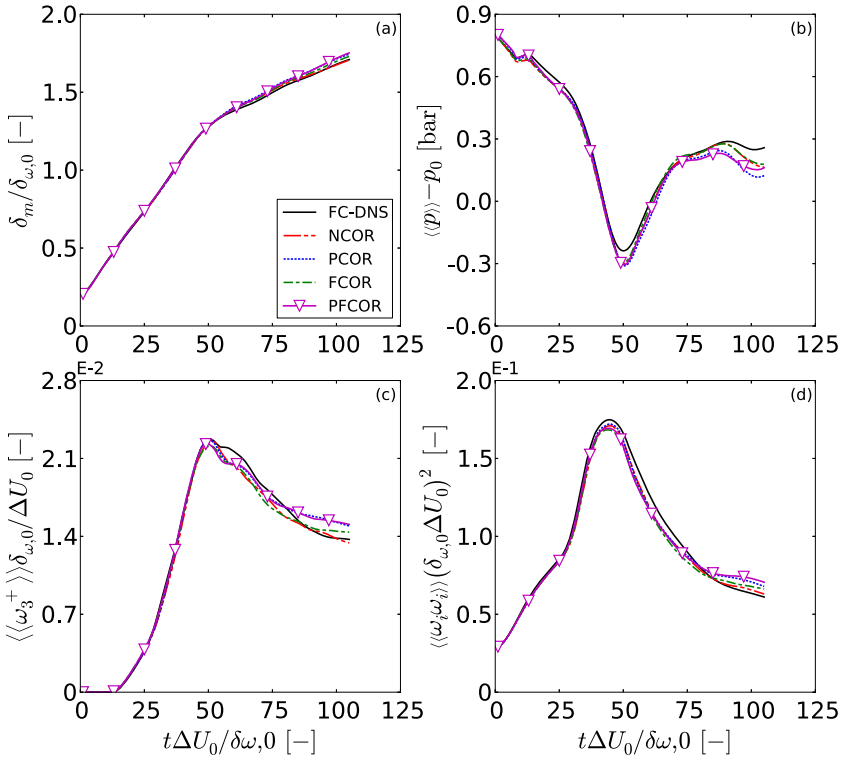

FIG. 10. Timewise evolution of (a) $\delta_m/\delta_{\omega,0}$, (b) $(\langle\langle p\rangle\rangle - p_0)$, (c) $\langle\langle\omega_3^+\rangle\rangle$ $(\delta_{\omega,0}/\Delta U_0)$, and (d) $\langle\langle\omega_i\omega_i\rangle\rangle$ $(\delta_{\omega,0}/\Delta U_0)^2$ for p60 from the FC-DNS and several LES using different SGS models.

the SLA model while at $\overline{\Delta} = 6\Delta x$ the reduction is typically 50%. An even larger effect is seen on Fig. 7 for $\nabla\cdot[\overline{p(\phi)}\widetilde{\mathbf{u}} - \nabla\cdot\overline{p(\phi)}_{\mathrm{mod}}\widetilde{\mathbf{u}}]$. The rms of this term displays a double-hump feature and the overwhelming activity is associated again with the upper part of the mixing layer. The ILA model for $\overline{p(\phi)}$ reduces the rms of $\nabla\cdot[\overline{p(\phi)}\widetilde{\mathbf{u}} - \nabla\cdot\overline{p(\phi)}_{\mathrm{mod}}\widetilde{\mathbf{u}}]$ with respect to that computed using the SLA by more than a factor of two except for $\overline{\Delta} = 6\Delta x$ in the region of maximum activity, independently of the values of p_0 and $\overline{\Delta}$.

The rms results displayed on Fig. 8 for $(\nabla\cdot\overline{\mathbf{J}_{C_7H_{16}}(\phi)} - \nabla\cdot\overline{\mathbf{J}_{C_7H_{16}}(\phi)}_{\mathrm{mod}})$ and $(\nabla\cdot\overline{\mathbf{J}_{H_2O}(\phi)} - \nabla\cdot\overline{\mathbf{J}_{H_2O}(\phi)}_{\mathrm{mod}})$ show similarities between the behavior of n-C_7H_{16} and that of H_2O. The ILA model performs well for both n-C_7H_{16} and H_2O, leading to an error reduction of approximately a third compared to the corresponding SLA, despite the rms for n-C_7H_{16} being $O(10^2) - O(10^3)$ larger than that of H_2O. For both species, the rms increases by approximately a factor of 2 when $\overline{\Delta}$ increases by the same factor. A significant difference between n-C_7H_{16} and H_2O is that whereas the rms obtained with SLA and ILA varies for n-C_7H_{16} according to $\overline{\Delta}$, for H_2O no such dependence on $\overline{\Delta}$ can be seen. We attribute this finding for H_2O to the fact that its initial distribution being uniform rather than segregated as that of n-C_7H_{16}, the gradients of the former are considerably smaller and thus filtering at a larger $\overline{\Delta}$ has only minimal effect on the amount of activity removed.

Finally, the examination of Fig. 9 for $\overline{\nabla\cdot\mathbf{q}(\phi)}$ reveals that the rms increases approximately proportionally with p_0. At larger $\overline{\Delta}$, the ILA model is not as effective as at smaller $\overline{\Delta}$, a fact which is expected for quantities with very large non-uniformities, and the ILA model also seems slightly less effective at the larger p_0.

C. *A posteriori* assessment of SGS models for $\overline{p(\phi)}$, $\overline{\mathbf{q}(\phi)}$, and $\overline{\mathbf{J}_\alpha(\phi)}$ in LES

The performance of the models for $\overline{p(\phi)}$, $\overline{\mathbf{q}(\phi)}$, and $\overline{\mathbf{J}_\alpha(\phi)}$ described in Sec. IV B 2 is evaluated here by conducting LESs of the mixing layers described in Table II. In all simulations, the LES grid

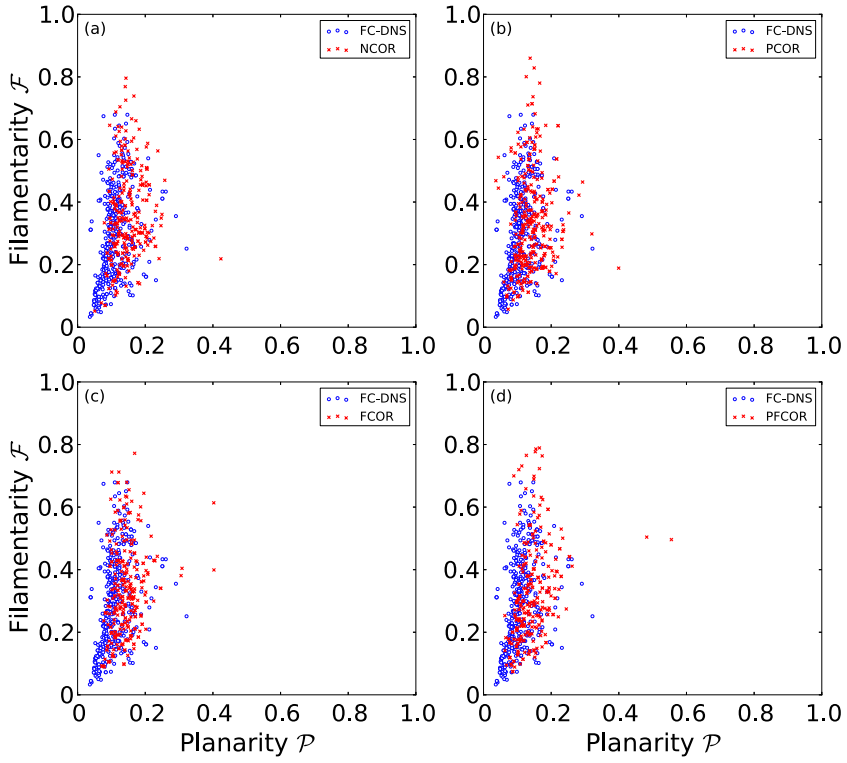

FIG. 11. Comparison of the scatter plot of the filamentarity versus planarity at t_{tr}^{*} for II_d iso-surfaces obtained in p60 LESs conducted with $\Delta x_{LES} = 3\Delta x$, $\overline{\Delta} = 2\Delta x_{LES} = 6\Delta x$, and $\widehat{\Delta} = 2\overline{\Delta}$ and different models for the unconventional SGS terms.

spacing is $\Delta x_{\mathrm{LES}} = 3\Delta x$; additionally, $\overline{\Delta} = 2\Delta x_{\mathrm{LES}} = 6\Delta x$ and $\hat{\Delta} = 2\overline{\Delta} = 12\Delta x$. The LES results are compared with those obtained from the corresponding FC-DNS solutions. The numerics of the LES code is substantially the same as that used in the DNS code. In DNS, one uses a high-order low-pass filter[23] to maintain long-time stability. This filter, being of high order, only removes spurious information without affecting the physical content of the data as the filter only acts on the smallest scales that can be resolved on the grid and thus does not act as a turbulence model which could allow under-resolved simulations; for the well-resolved DNS grid, the frequency of the high-order filtering does not alter the solution. Since the LES grid resolution is only sufficient to resolve the large scales, to guarantee the numerical stability of the simulations,[23] filtering of the solution fields using a very high-order low-pass filter was performed at regular intervals Δt_{filt} of the simulation time, with $\Delta t_{\mathrm{filt}} = 3\Delta x_{\mathrm{LES}}/(\Delta U_0/Ma_0)$. This value of Δt_{filt} seems a natural fit for these LESs, although, unlike in DNS, the filtering frequency is expected to slightly affect the solution; this is in concert with LES being an approximation of the exact flow field.

The initial and boundary conditions for LES were obtained by spatially filtering and coarsening those of the corresponding DNS.

In all LESs presented here, the Dynamic Mixed Gradient (DMG) model is used for the turbulent SGS fluxes τ_{ij}, ζ_j, $\eta_{\alpha j}$.[13,43] For the purpose of performing *a posteriori* computations using the DMG model, we consider the filter width $\widehat{\overline{\Delta}}$ corresponding to the double convolution of the two filters having filter widths $\overline{\Delta}$ and $\widehat{\Delta}$, and following Vreman *et al.*,[44] we compute

$$\widehat{\overline{\Delta}}^2 = \widehat{\Delta}^2 + \overline{\Delta}^2, \tag{52}$$

as an approximation to the exact value of $\widehat{\overline{\Delta}}^2$. Modeling of $\overline{p(\phi)}$, $\overline{\mathbf{q}(\phi)}$, and $\overline{\mathbf{J}_\alpha(\phi)}$ is based on four different approaches, labeled as NCOR, PCOR, FCOR, and PFCOR, respectively. NCOR uses the standard LES assumptions for all these terms; PCOR (FCOR) uses the model for $\overline{p(\phi)}$ ($\overline{\mathbf{J}_\alpha(\phi)}$ and

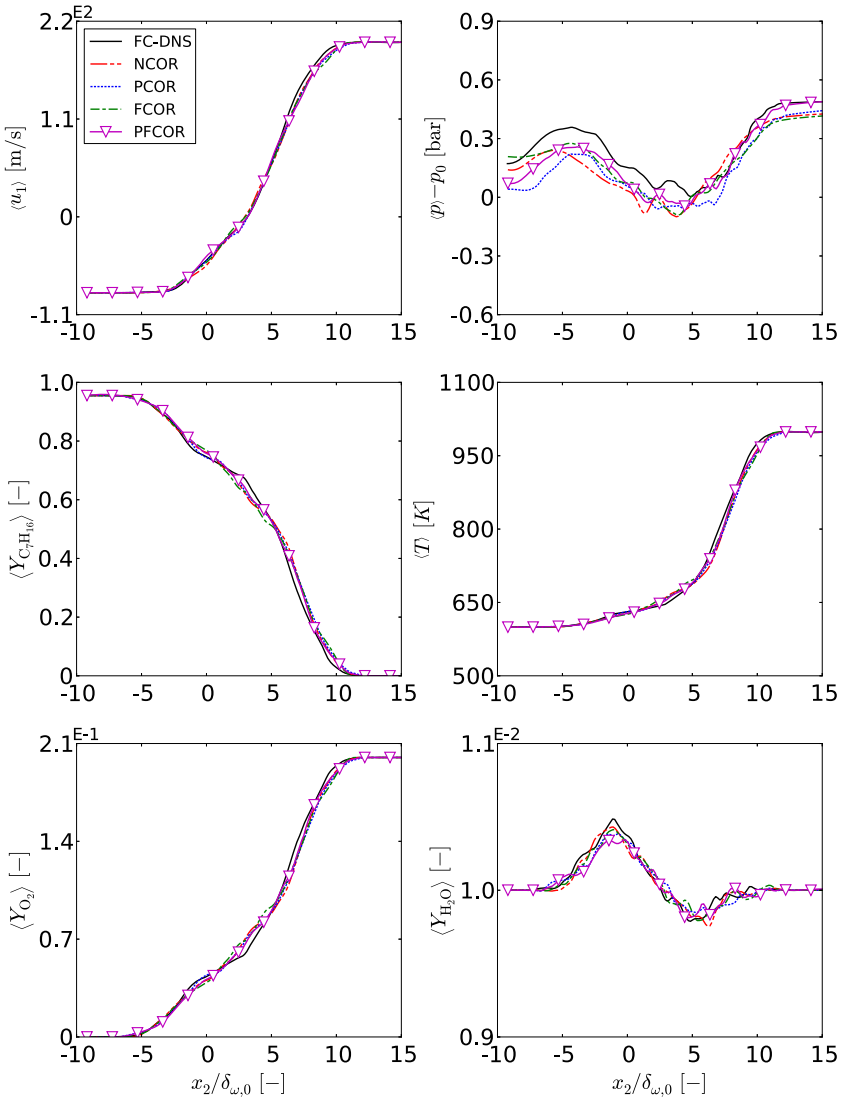

FIG. 12. Cross-stream variation of homogeneous plane averages of dynamic and thermodynamic variables at t^*_{tr}. The comparison is between the LESs with models NCOR, PCOR, FCOR, and PFCOR and the FC-DNS for simulation p60.

$\overline{\mathbf{q}(\phi)}$) presented in Sec. IV B 2, while the standard LES assumptions are used for the remaining unconventional SGS terms; and PFCOR uses the models given in Sec. IV B 2 for $\overline{p(\phi)}$, $\overline{\mathbf{q}(\phi)}$, and $\overline{\mathbf{J}_\alpha(\phi)}$. Results are examined from the viewpoint of time-wise evolution of domain averages, statistical measures at t^*_{tr} provided by $\mathcal{F}$ versus $\mathcal{P}$ for II_d, cross-stream variation of homogeneous-plane averages and homogeneous-plane averages of second-order correlations of interest at t^*_{tr}, and visualizations of thermodynamic variables at t^*_{tr}.

1. Integral quantities

Fig. 10 shows the temporal evolution of the normalized momentum thickness δ_m, the domain-averaged positive spanwise vorticity $\langle\langle \omega_3^+ \rangle\rangle$, and the domain-averaged enstrophy $\langle\langle \omega_i \omega_i \rangle\rangle$; δ_m measures the growth of the mixing layer, $\langle\langle \omega_3^+ \rangle\rangle$ is an indicator of the small-scales formation in the layer (initially, ω_3 is negative at all spatial locations), and $\langle\langle \omega_i \omega_i \rangle\rangle$ is a manifestation of the stretching and twisting aspects of turbulence. The results indicate that these quantities are all excellently predicted by the different LES models tested, and the peak vortical quantities are most accurately predicted

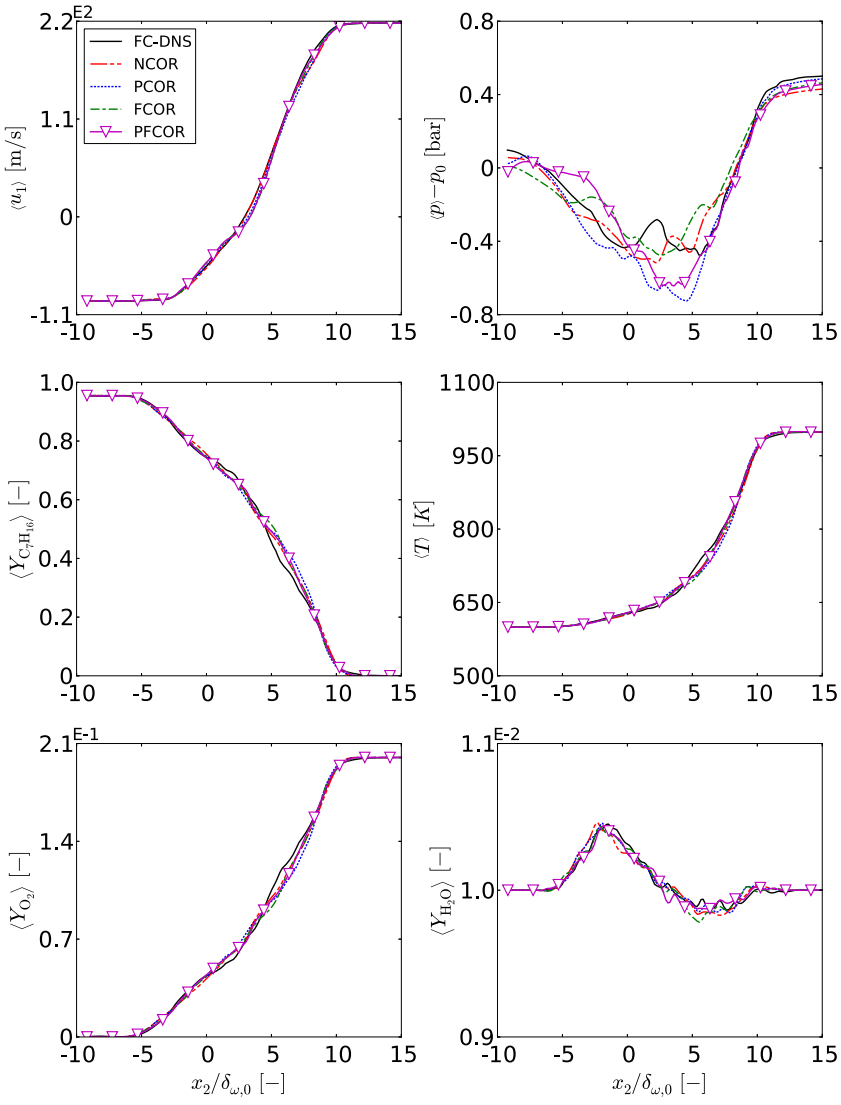

FIG. 13. Cross-stream variation of homogeneous plane averages of dynamic and thermodynamic variables at t^*_{tr}. The comparison is between the LESs with models NCOR, PCOR, FCOR, and PFCOR and the FC-DNS for simulation p80.

by NCOR and PCOR. Another quantity of interest is the difference between the domain-averaged pressure and p_0, $(\langle\langle p\rangle\rangle - p_0)$. For models PCOR and PFCOR, p is computed using the model of Sec. IV B 2, as without this correction smaller-p values are obtained. All four models predict very well the pressure evolution. Of note, at the latter times of the simulation, it appears that the NCOR and FCOR models more faithfully reproduce the FC-DNS than the other models as far as the vorticity and pressure aspects of the flow.

Thus, from the viewpoint of the integral quantities, it would seem that at the relatively small Reynolds numbers achievable in DNS and the relatively small filter width chosen here, in LES of high-p and multi-species mixing flows, there is no predictive advantage in using models for $\overline{p(\phi)}$, $\overline{\mathbf{q}(\phi)}$, and $\overline{\mathbf{J}_\alpha(\phi)}$ different from the SLA. Similar results are obtained for p80 (not shown).

2. Morphology of the large-scale structures of the flow at t^*_{tr}

The $(\mathcal{P}, \mathcal{F})$ scatter plots of the II_d iso-surfaces extracted at t^*_{tr} from the various LESs are shown in Fig. 11 for p60, as an example; the results for p80 are similar. All LES models have comparable

success in reproducing the morphological features of the flows associated with the second invariant of the deformation rate tensor. This is an encouraging result, meaning that discrimination among LES models should rely on other features of the flow.

3. Homogeneous-plane averages and second-order correlations at t^*_{tr}

Homogeneous-plane averages of the streamwise velocity and of thermodynamic variables appear in Figs. 12 and 13 for simulations p60 and p80, respectively. For both simulations, $\langle u_1 \rangle, \langle T \rangle$, $\langle Y_{C_7H_{16}} \rangle$ and $\langle Y_{O_2} \rangle$ are excellently predicted by all LES models. We also notice the success in the main-feature prediction of $\langle Y_{H_2O} \rangle$ despite it being a very small quantity, and the fact that all LES models return the value of the freestreams; the very small fluctuations in the mixing layer, due to multi-species diffusion, are not necessarily rendered accurately by the models. The largest discrepancy between the predictions of the LES models and the FC-DNS and also among LES models occurs for $(\langle p \rangle - p_0)$. For the p60 simulation, PFCOR is the only model able to recover the freestream value in the upper stream and seems closer overall to the FC-DNS although the lower stream value is not well captured. For the p80 simulation, the upper stream value and lower stream values are well predicted by several models, but overall NCOR seems to be more closely following the FC-DNS.

Faced with the uncertainty in visually discriminating among LES models to assign relative accuracy, we define for any variable Ψ the error

$$\varepsilon_\Psi \equiv \frac{\int_{-L_2}^{L_2} |\Psi_{LES}(x_2) - \Psi_{FC-DNS}(x_2)|\, dx_2}{\int_{-L_2}^{L_2} |\Psi_{FC-DNS}(x_2)|\, dx_2} \tag{53}$$

which provides an overall measure of a LES-model performance for Ψ by comparing with the FC-DNS. Results from computations using Eq. (53) are presented for p80 in Table XI for all averaged variables. Also listed are the most accurate and second most-accurate model, with the idea that if the most accurate model is not the same but the second most-accurate model is the same, the latter model would be recommended. The most accurate predictions are made for all LES models for T, p, Y_{CO_2}, and Y_{H_2O}. In the next best-predicted category of variables are $\rho, u_1, Y_{C_7H_{16}}$, and Y_{O_2}. Finally, the most inaccurate predictions are made for u_2 and u_3. Clearly, there is wide-spread capability among the models and thus it is generally difficult to recommend one LES model over another. One may take the position that since the NCOR model is the most computationally efficient, since it is the most accurate for predicting p, u_1, u_2, and since it is the second most-accurate for predicting the major species, this model should that of choice. Another position is that a simulation should be judged according to the least accurately predicted variable and then a model including the ILA should be used, in which case the prediction of other variables may also be improved.

TABLE XI. Error ε_Ψ computed for the homogeneous-plane-averaged variables obtained with different LES models for p80. "Best" is defined as "most accurate."

	NCOR	PCOR	FCOR	PFCOR	Best model	Second-best model
$\langle \rho \rangle$	0.201×10^{-1}	0.218×10^{-1}	0.183×10^{-1}	0.149×10^{-1}	PFCOR	FCOR
$\langle T \rangle$	0.465×10^{-2}	0.693×10^{-2}	0.464×10^{-2}	0.445×10^{-2}	PFCOR	FCOR
$\langle p \rangle$	0.795×10^{-3}	0.189×10^{-2}	0.103×10^{-2}	0.190×10^{-2}	NCOR	FCOR
$\langle u_1 \rangle$	0.114×10^{-1}	0.157×10^{-1}	0.162×10^{-1}	0.160×10^{-1}	NCOR	PCOR
$\langle u_2 \rangle$	0.910×10^{-1}	0.788×10^{-1}	0.127×10^{0}	0.123×10^{0}	NCOR	PCOR
$\langle u_3 \rangle$	0.804×10^{0}	0.755×10^{0}	0.827×10^{0}	0.777×10^{0}	PCOR	PFCOR
$\langle Y_{H_2O} \rangle$	0.270×10^{-2}	0.220×10^{-2}	0.230×10^{-2}	0.206×10^{-2}	PFCOR	PCOR
$\langle Y_{CO_2} \rangle$	0.240×10^{-2}	0.221×10^{-2}	0.190×10^{-2}	0.200×10^{-2}	FCOR	PFCOR
$\langle Y_{O2} \rangle$	0.212×10^{-1}	0.290×10^{-1}	0.217×10^{-1}	0.184×10^{-1}	PFCOR	NCOR
$\langle Y_{C_7H_{16}} \rangle$	0.198×10^{-1}	0.270×10^{-1}	0.204×10^{-1}	0.171×10^{-1}	PFCOR	NCOR

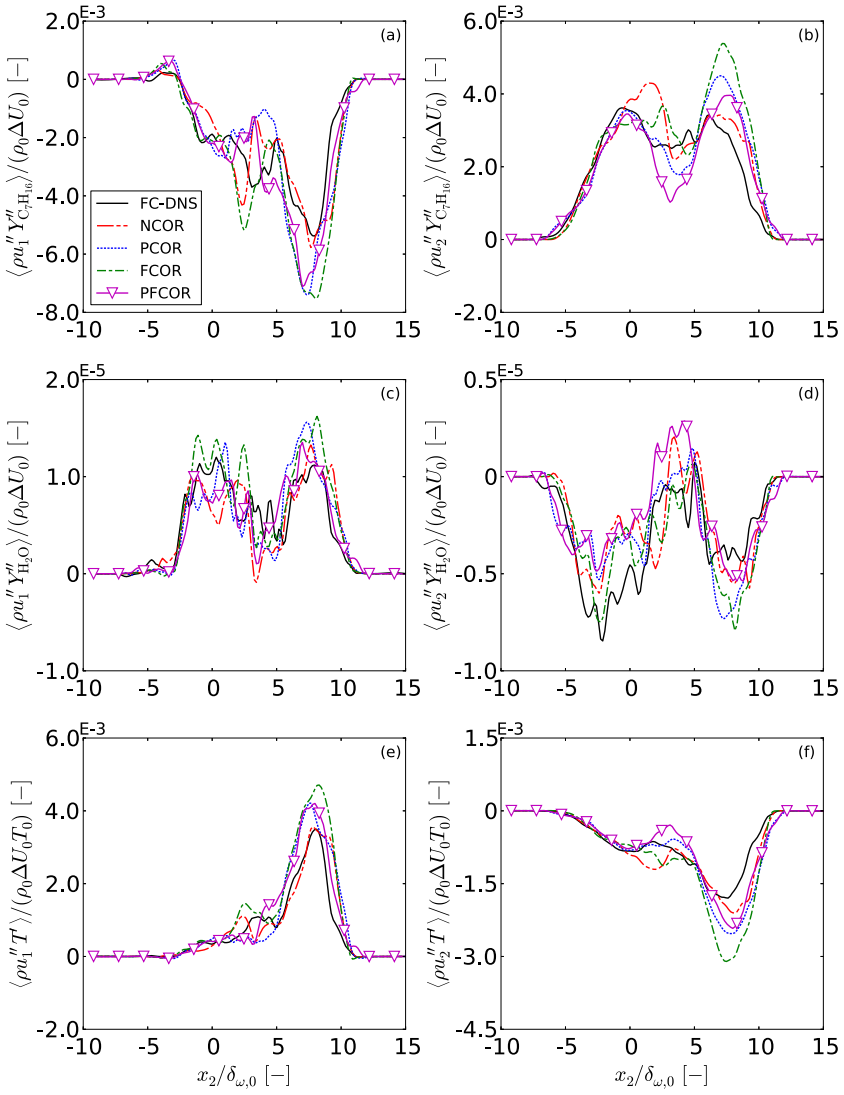

FIG. 14. Cross-stream variation of non-dimensional second-order correlations for p60 at t_{tr}^*. (a) $\langle \rho u_1'' Y''_{C_7H_{16}} \rangle$, (b) $\langle \rho u_2'' Y''_{C_7H_{16}} \rangle$, (c) $\langle \rho u_1'' Y''_{H_2O} \rangle$, (d) $\langle \rho u_2'' Y''_{H_2O} \rangle$, (e) $\langle \rho u_1'' T'' \rangle$, and (f) $\langle \rho u_2'' T'' \rangle$. Comparison is made between the FC-DNS and four LESs conducted with different models for the unconventional SGS terms.

Trying to further discriminate among LES models, second-order correlations are considered since they are more difficult to predict with accuracy. By definition, $f'' = f - \langle f \rangle$, with f representing a generic field. Samples of the results, i.e., $\langle \rho u_1'' Y''_{C_7H_{16}} \rangle$, $\langle \rho u_2'' Y''_{C_7H_{16}} \rangle$, $\langle \rho u_1'' Y''_{H_2O} \rangle$, $\langle \rho u_2'' Y''_{H_2O} \rangle$, $\langle \rho u_1'' T'' \rangle$, and $\langle \rho u_2'' T'' \rangle$, are illustrated in Fig. 14 for p60 and in Fig. 15 for p80, both at t_{tr}^*. Whereas the general variation of each variable is well captured by all LES models, the small-scale structure is again not entirely captured by the models, although with increasing p_0, one generally observes less deviation from the FC-DNS. To obtain a quantitative assessment of the performance of all LES models, we compute ε_Ψ for each of the second-order correlations; the results for p80 are listed in Table XII. As expected, it is much more difficult to accurately predict the second-order correlations than the planar averages: the errors are generally in Table XII one order of magnitude larger than in Table XI. The model which minimizes the error is either PCOR or NCOR.

These results indicate that, in LES of high-p multi-species mixing flows, at the relatively small Reynolds numbers attainable in DNS and the relatively small filter chosen for this scientific study, there is no definite benefit in using the models for $\overline{p(\phi)}$, $\overline{\mathbf{q}(\phi)}$, and $\overline{\mathbf{J}_\alpha(\phi)}$ developed in Sec. IV B 2

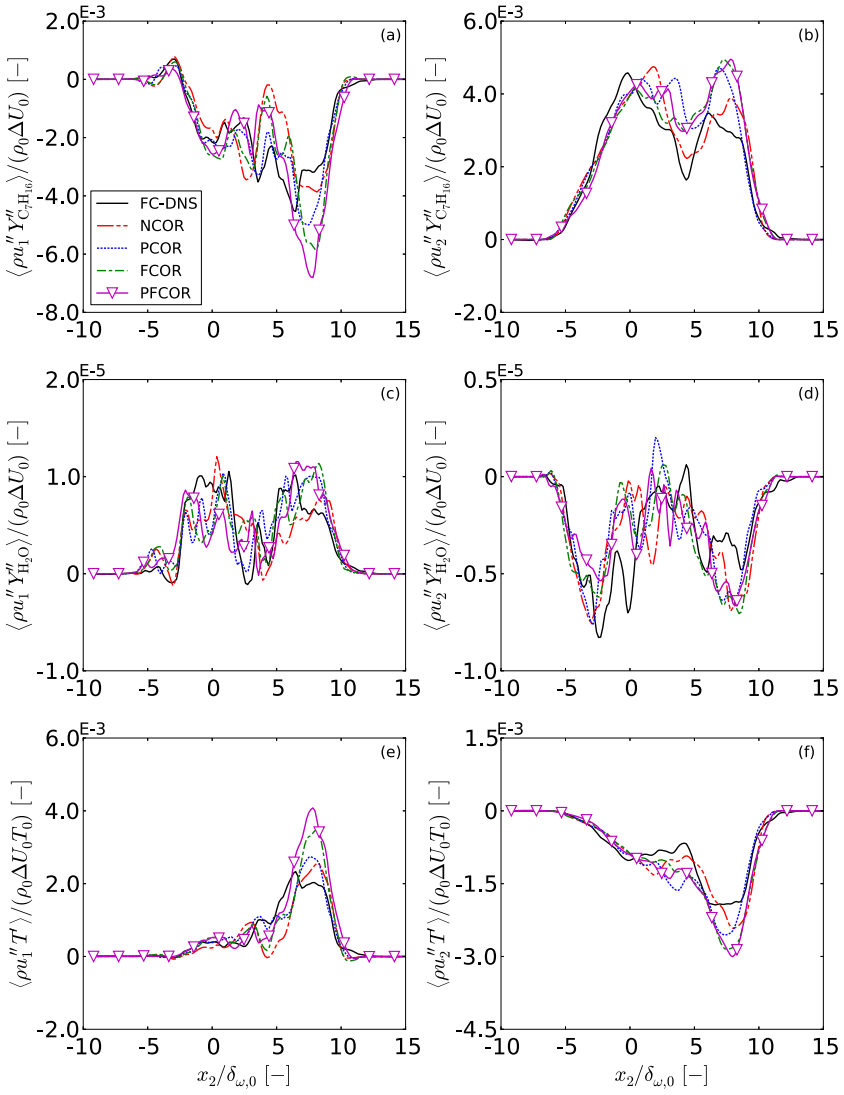

FIG. 15. Cross-stream variation of non-dimensional second-order correlations for p80 at t^*_{tr}. (a) $\langle \rho u_1'' Y''_{C_7H_{16}} \rangle$, (b) $\langle \rho u_2'' Y''_{C_7H_{16}} \rangle$, (c) $\langle \rho u_1'' Y''_{H_2O} \rangle$, (d) $\langle \rho u_2'' Y''_{H_2O} \rangle$, (e) $\langle \rho u_1'' T'' \rangle$, and (f) $\langle \rho u_2'' T'' \rangle$. Comparison is made between the FC-DNS and four LESs conducted with different models for the unconventional SGS terms.

compared to employing the standard LES assumptions. These conclusions are different from those obtained for binary-species high-p mixing[13,14] and indicate that care should be taken not to infer properties of multi-species mixing from binary-species experiments.

4. *Visualizations of thermodynamic quantities at t^*_{tr}*

The LESs presented in this work share the same initial and boundary conditions. As such, these simulations are deterministic in nature; this feature is used here to evaluate the various LESs' models for $\overline{p(\phi)}$, $\overline{\mathbf{J}_\alpha(\phi)}$, and $\overline{\mathbf{q}(\phi)}$ by comparing the contours of several thermodynamics variables at t^*_{tr}. Because the simulations are deterministic, it is expected that, with appropriate modeling of the unclosed terms, the LES fields should not differ much from those of the FC-DNS. To show that despite the errors listed in Tables XI and XII, the LESs reproduce remarkably well the general features of the FC-DNS, we display in Fig. 16, as an example, the T field in the $x_3 = L_3/16$ plane. The FC-DNS is illustrated in Fig. 16(a) and compared to it are the NCOR LES in Fig. 16(b), PCOR LES

TABLE XII. Error ε_Ψ computed for the second-order correlations using the databases obtained with different LES models for p80. "Best" is defined as "most accurate."

	NCOR	PCOR	FCOR	PFCOR	Best model	Second-best model
$\langle \rho u_1'' Y_{H_2O}'' \rangle$	0.473×10^0	0.417×10^0	0.508×10^0	0.540×10^0	PCOR	NCOR
$\langle \rho u_2'' Y_{H_2O}'' \rangle$	0.527×10^0	0.530×10^0	0.482×10^0	0.481×10^0	PFCOR	FCOR
$\langle \rho u_3'' Y_{H_2O}'' \rangle$	0.127×10^1	0.141×10^1	0.131×10^1	0.174×10^1	NCOR	FCOR
$\langle \rho u_1'' Y_{C_7H_{16}}'' \rangle$	0.421×10^0	0.259×10^0	0.447×10^0	0.456×10^0	PCOR	NCOR
$\langle \rho u_2'' Y_{C_7H_{16}}'' \rangle$	0.197×10^0	0.246×10^0	0.251×10^0	0.265×10^0	NCOR	PCOR
$\langle \rho u_3'' Y_{C_7H_{16}}'' \rangle$	0.166×10^1	0.151×10^1	0.192×10^1	0.197×10^1	PCOR	NCOR
$\langle \rho u_1'' T' \rangle$	0.434×10^0	0.283×10^0	0.481×10^0	0.527×10^0	PCOR	NCOR
$\langle \rho u_2'' T' \rangle$	0.230×10^0	0.271×10^0	0.303×10^0	0.325×10^0	NCOR	PCOR
$\langle \rho u_3'' T' \rangle$	0.203×10^1	0.157×10^1	0.207×10^1	0.218×10^1	PCOR	NCOR
$\langle \rho u_1'' p' \rangle$	0.653×10^0	0.660×10^0	0.978×10^0	0.115×10^1	NCOR	PCOR
$\langle \rho u_2'' p' \rangle$	0.763×10^0	0.643×10^0	0.632×10^0	0.809×10^0	FCOR	PCOR
$\langle \rho u_3'' p' \rangle$	0.148×10^1	0.123×10^1	0.150×10^1	0.160×10^1	PCOR	NCOR

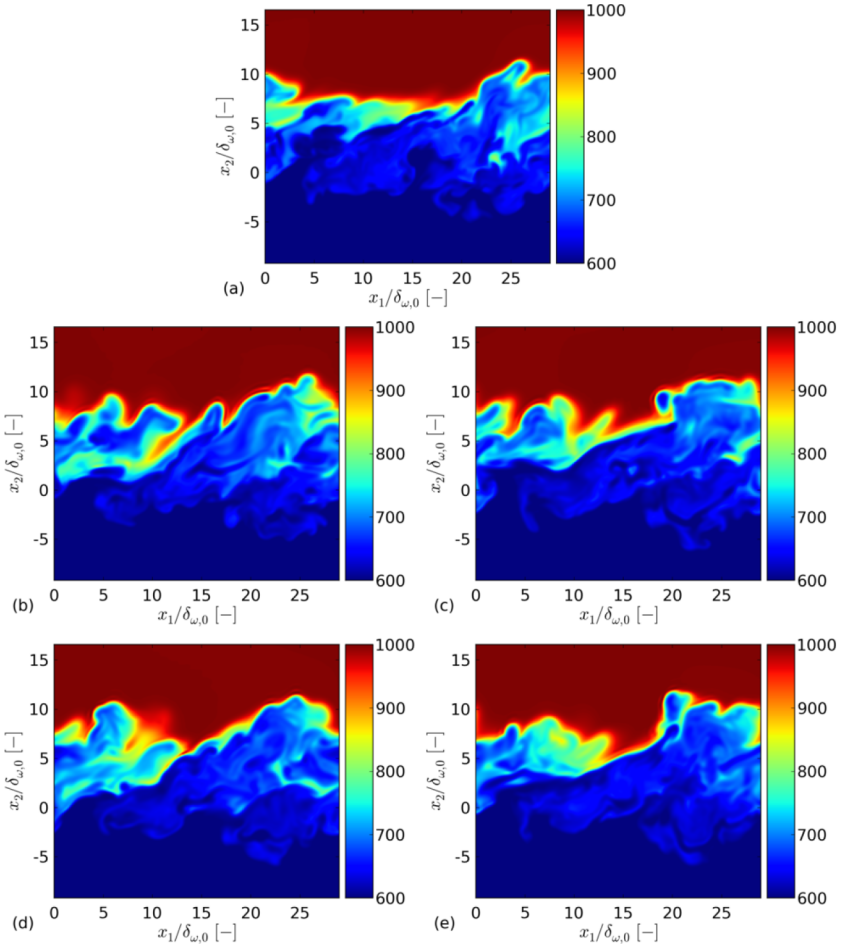

FIG. 16. Visualization of T obtained in p60 in the $x_3/L_3 = 1/16$ plane at t^*_{tr}. (a) FC-DNS, (b) NCOR, (c) PCOR, (d) FCOR, and (e) PFCOR.

in Fig. 16(c), FCOR LES in Fig. 16(d), and PFCOR LES in Fig. 16(e). All models are successful in duplicating the relative regions of high and low T and even some smaller scale structures of the T distribution. These visualizations are typical of the success in duplicating the primitive variables.

V. SUMMARY AND CONCLUSIONS

A DNS database describing multi-species mixing under supercritical-pressure (supercritical-p) conditions was created to conduct an *a priori* analysis and an *a posteriori* assessment regarding the modeling of some of the unclosed terms that appear in the equations for LES. The goal of the study was to propose models for the unclosed terms of the LES conservation equations other than the terms stemming from the convective terms of the original equations and to determine whether these models are helpful in producing more accurate LES than the standard model in which these terms are computed using the same functional form as in the original conservation equations. The configuration considered was that of a temporally evolving mixing layer between a stream containing n-heptane and a stream containing nitrogen and oxygen, each stream being vitiated with carbon dioxide and water. Two cases were simulated: the initial values of the Reynolds number for these simulations were the same, whereas different values for the freestream pressure (p_0) were used. Most of the analysis was conducted at the transitional time, i.e., the flow time corresponding to transition from laminar conditions to a flow displaying turbulent characteristics. In post-processing the results, the DNS data were filtered using a top-hat filter with two different values of the filter width $\overline{\Delta}$, $\overline{\Delta} = 3\Delta x$, and $\overline{\Delta} = 6\Delta x$, where Δx is the DNS grid spacing; despite being relatively small, these values of $\overline{\Delta}$ correspond to coarse-grid LES for the present transitional flow.

Because it is expected that accurate LES solution fields should contain large-scale structures having levels of morphological complexity similar to those of the structures observed in the FC-DNS fields, we examined the morphological properties of the iso-surfaces of the second invariant of the rate of deformation tensor (II_d) and the irreversible entropy production rate (g), both computed using either the DNS solution fields or their FC-DNS counterparts. MFs provided information on the planarity ($\mathcal{P}$) and the filamentarity ($\mathcal{F}$). Examination of the DNS database revealed that the iso-surfaces of g have more complex structure than those of II_d. With increasing p_0, the morphological complexity of both II_d and g iso-surfaces slightly decreased as manifested by a narrower range of $\mathcal{P}$ and $\mathcal{F}$ values. The iso-surfaces of II_d were mainly filamentary whereas those of g had more diverse shape characteristics. Although the FC-DNS iso-surfaces had less structural complexity than those of the DNS, the aspect of the g structures was found to be more complex than that of the II_d structures. This information indicated that modeling of SGS terms related to the thermodynamic variables may be potentially important.

Thus, in an *a priori* study, we proposed different models for three unclosed terms that appear in the LES equations: the filtered pressure $\overline{p(\phi)}$, the filtered heat flux $\overline{\mathbf{q}(\phi)}$, and the filtered species fluxes $\overline{\mathbf{J}_\alpha(\phi)}$. The analysis of the domain-averaged rms of all terms that appear in the LES equations, computed using the DNS database, revealed that, for the flows under consideration in this study, if $\overline{p(\phi)}$, $\overline{\mathbf{q}(\phi)}$, and $\overline{\mathbf{J}_\alpha(\phi)}$ were to be computed as $p(\overline{\phi})$, $\mathbf{q}(\overline{\phi})$, and $\mathbf{J}_\alpha(\overline{\phi})$, a significant loss of accuracy could be expected in some regions of the mixing layers. Improved models for $\overline{p(\phi)}$, $\overline{\mathbf{q}(\phi)}$, and $\overline{\mathbf{J}_\alpha(\phi)}$ were thus formulated using a scale-similarity approach. *A priori* testing of these new models revealed that, for the flow conditions considered in this study, they usually perform significantly better than the standard closures $\overline{p(\phi)} = p(\overline{\phi})$, $\overline{\mathbf{q}(\phi)} = \mathbf{q}(\overline{\phi})$, and $\overline{\mathbf{J}_\alpha(\phi)} = \mathbf{J}_\alpha(\overline{\phi})$ that are often used in LES of flows described by a perfect gas equation of state. The above findings were independent of the value of p_0 and of the filter width considered. For some of the terms considered in the analysis, the error reduction seemed unaffected by the value of the filter width.

The *a posteriori* evaluation of the improved models for $\overline{p(\phi)}$, $\overline{\mathbf{q}(\phi)}$, and $\overline{\mathbf{J}_\alpha(\phi)}$ was conducted using the dynamic mixed gradient model to close the conventional turbulent SGS fluxes in all LESs, while modeling of the unconventional SGS terms was based on four different approaches in which either the standard model, or one or several of the improved models were used. These simulations were conducted using a grid spacing $\Delta x_{\mathrm{LES}} = 3\Delta x$ and with $\overline{\Delta} = 2\Delta x_{\mathrm{LES}}$. All four LES approaches were very accurate in reproducing the temporal evolutions of the layer thickness, of

the vortical flow characteristics and the volume-averaged pressure, the morphological aspects of the flow and the general features of the cross-stream variation of the homogeneous-plane averages, and of second-order correlations. However, none of the models was clearly superior in capturing the small-scale features of the cross-stream profiles. Evaluations based on relative errors compared to the FC-DNS confirmed the visual observations.

It is well-known that the full potential of SGS models is only attainable at the larger Reynolds numbers and large filter widths encountered in practical applications. From the viewpoint of conducting LES of high-p multi-species mixing, this study indicates that at relatively small Reynolds numbers achievable in DNS and relatively small filter widths, the computationally efficient LES model based on the standard LES assumptions is viable. This study also provided options for practical applications in which the Reynolds number is much larger and the filter width is very large, and thus the activity of the unconventional SGS terms could dominate in the conservation equations, thereby requiring the utilization of the improved-LES-assumption models developed herein.

ACKNOWLEDGMENTS

This study was conducted at the Jet Propulsion Laboratory (JPL) of the California Institute of Technology (Caltech), and this material is based upon work supported by the U.S. Department of Energy, Office of Science, Office of Basic Energy Sciences (Gas Phase Chemical Physics in the Chemical Sciences, Geosciences and Biosciences Division) under Award No. DE-SC0002679, and the direction of Dr. Wade Sisk and Dr. Mark Pederson. The computational resources were provided by the National Energy Research Supercomputing Center of the Department of Energy, by the NASA Advanced Supercomputing at Ames Research Center, and by the JPL Supercomputing Center.

APPENDIX A: TRANSPORT PROPERTIES

Unlike for atmospheric-p flows where three transport properties are generally sufficient (viscosity, diffusivity, and thermal conductivity) for high-p conditions, there are four relevant transport properties.

1. Mixture viscosity

To compute the individual species viscosity, μ_α^{vis}, the Lucas method[45] has been selected due to its high-p-accuracy capabilities. To compute the mixture physical viscosity, μ_{ph}, the Wilke method[45] is utilized providing

$$\mu_{ph} = \sum_{\alpha=1}^{N} X_\alpha \omega_\alpha^M \mu_\alpha^{vis}, \tag{A1}$$

$$(\omega_\alpha^M)^{-1} = \sum_{\beta=1}^{N} \phi_{\alpha\beta} X_\beta, \tag{A2}$$

$$\phi_{\alpha\beta} = \frac{\left[1 + (\mu_\alpha^{vis}/\mu_\beta^{vis})^{1/2}(m_\beta/m_\alpha)^{1/4}\right]^2}{\left[8(1 + m_\alpha/m_\beta)\right]^{1/2}}, \tag{A3}$$

where ω_α^M are the weighting factors.[45] We distinguish between μ_{ph}, the reference viscosity μ_R defined in Sec. III, and the computational viscosity μ used to enable resolution to scales of $O(\eta_K)$, as explained in Sec. III.

2. Mixture thermal conductivity

To compute the physical mixture thermal conductivity, λ_{ph}, first the species conductivities λ_α are calculated using the Stiel-Thodos method,[45] and then the Wassiljewa-Mason-Saxena method[45] is

utilized to compute λ_{ph} from λ_α as

$$\lambda_{ph} = \sum_{\gamma=1}^{N} X_\alpha \omega_\alpha^Q \lambda_\alpha, \tag{A4}$$

where

$$\omega_\alpha^Q = \omega_\alpha^M. \tag{A5}$$

In Sec. III, we explain how a scaled thermal conductivity, λ, is computed that is used to perform DNS.

3. Binary mass diffusivities

Matrix elements $\mathcal{D}^b_{\alpha\gamma}$ are the building blocks of $\mathbb{D}_{\alpha\gamma}$ and ultimately of $D'_{\alpha\gamma}$. To compute $\mathcal{D}^b_{\alpha\gamma} = \mathcal{D}_{\alpha\gamma}$, we adopt the method of Harstad and Bellan[46] which gives (in cgs units)

$$n\mathcal{D}_{\alpha\gamma} = 2.81 \times 10^{-5} \frac{f_{D,\alpha\gamma}(T)}{r_D v_{c,\alpha\gamma}^{2/3}} \left[\left(\frac{1}{m_\alpha} + \frac{1}{m_\gamma} \right) T \right]^{1/2}, \tag{A6}$$

where $f_{D,\alpha\gamma}(T)$ is generically defined for each matrix element as $f_D(T) \equiv (T_{red})^s$ with $\ln s = \sum_{\zeta=0}^{5} a_\zeta^s (\ln T_{red})^\zeta$ where the a^s vector has elements $\{-0.842\,11, -0.326\,43, -0.100\,53, 0.077\,47, 0.0127, -0.009\,95\}$, and r_D is a constant $O(1)$ which provides an empirical adjustment for the specifics of the collisional interactions of a selected pair of species. $T_{red,\alpha\gamma} \equiv T/T_{c,\alpha\gamma}$ with

$$T_{c,\alpha\gamma} = (1 - k_{\alpha\gamma}) \sqrt{T_{c,\alpha} T_{c,\gamma}} \quad \text{with } k_{\alpha\alpha} = 0, \tag{A7}$$

$$v_{c,\alpha\gamma} = \frac{1}{8} \left(v_{c,\alpha}^{1/3} + v_{c,\gamma}^{1/3} \right)^3, \tag{A8}$$

where $k_{\alpha\gamma}$ are the interaction coefficients used in the EOS; more details and values of $k_{\alpha\gamma}$ are provided elsewhere.[7] Values of r_D are listed in Harstad and Bellan[46] for species pairs relevant to combustion.

4. Binary thermal diffusion factors

According to Harstad and Bellan,[18]

$$\alpha^b_{T,\alpha\gamma} = \zeta_{\alpha\gamma} \frac{(m_\alpha \omega_\gamma^T - m_\gamma \omega_\alpha^T)}{(m_\alpha + m_\gamma)\mathcal{D}_{\alpha\gamma}}, \tag{A9}$$

$$\omega_\alpha^T = \frac{\omega_\alpha^Q \lambda_\alpha}{R_u n}, \quad \zeta_{\alpha\gamma} = \frac{6}{5} C^*_{\alpha\gamma} - 1, \tag{A10}$$

where ω_α^Q is computed from Eqs. (A2) to (A5), and $C^*_{\alpha\gamma}$ is given by Hishfelder *et al.*[19] and is function of a normalized temperature including the characteristic molecular interaction potential as discussed by Harstad and Bellan.[18]

APPENDIX B: RELATIONSHIPS FOR THE EOS

Miscellaneous relationships relevant to the EOS are

$$a_{mix} = \sum_\alpha \sum_\gamma X_\alpha X_\gamma a_{\alpha\gamma}(T), \; b_{mix} = \sum_\alpha X_\alpha b_\alpha, \tag{B1}$$

where indices do not follow the Einstein notation, and

$$a_{\alpha\gamma} = (1 - k'_{\alpha\gamma}) \sqrt{\alpha_{\alpha\alpha} \alpha_{\gamma\gamma}}, \tag{B2}$$

TABLE XIII. Values of k' for species pairs. n_c is the number of C atoms in the species.

α	γ	k'
Alkane	Alkane	0.0
Alkane	N_2, O_2	0.15
Alkane	CO_2	0.11
Alkane	H_2O	$0.093\text{-}0.006n_c$
CO_2	H_2O	0.095
CO_2	N_2, O_2	−0.017
H_2O	N_2, O_2	0.17

$$\alpha_{\alpha\alpha}(T) \equiv 0.457\,236(R_u T_{c,\alpha})^2 \times \frac{\left[1 + c_\alpha(1 - \sqrt{T_{red,\alpha}})\right]^2}{p_{c,\alpha}}, \tag{B3}$$

$$c_\alpha = 0.374\,64 + 1.542\,26\Omega_\alpha - 0.269\,92\Omega_\alpha^2, \tag{B4}$$

where $T_{red,\alpha} \equiv T/T_{c,\alpha}$, $T_{c,\alpha}$ is the critical temperature and Ω_α is the acentric factor provided in Table I. Also,

$$b_\alpha = 0.077\,796\frac{R_u T_{c,\alpha}}{p_{c,\alpha}}, \tag{B5}$$

$$T_{c,\alpha\gamma} = \left(1 - k_{\alpha\gamma}\right)\sqrt{T_{c,\alpha}T_{c,\gamma}} \quad \text{with } k_{\alpha\alpha} = 0, \tag{B6}$$

$$v_{c,\alpha\gamma} = \frac{1}{8}\left(v_{c,\alpha}^{1/3} + v_{c,\gamma}^{1/3}\right)^3, \tag{B7}$$

$$Z_{c,\alpha\gamma} = \frac{1}{2}\left(Z_{c,\alpha} + Z_{c,\gamma}\right), \tag{B8}$$

$$p_{c,\alpha\gamma} = \frac{R_u T_{c,\alpha\gamma} Z_{c,\alpha\gamma}}{v_{c,\alpha\gamma n}}, \tag{B9}$$

with $T_{red,\alpha\gamma} \equiv T/T_{c,\alpha\gamma}$, $Z_{c,\alpha}$ being the critical compression factor with the compression factor defined as $Z = p/(\rho T R_u/m)$, $v_{c,\alpha}$ being the critical volume, and $p_{c,\alpha}$ being the critical pressure. $k_{\alpha\gamma}$ is an empirical mixing parameter. The relationship between parameters $k_{\alpha\gamma}$ and $k'_{\alpha\gamma}$ is

$$(1 - k_{\alpha\gamma}) = (1 - k'_{\alpha\gamma})\frac{(v_{c,\alpha}v_{c,\gamma})^{1/2}}{v_{c,\alpha\gamma}}\frac{Z_{c,\alpha\gamma}}{\sqrt{Z_{c,\alpha}Z_{c,\gamma}}}, \tag{B10}$$

and for all pairs not in Table XIII, $k'_{\alpha\gamma} = 0$ is used.

[1] T. Edwards, "Cracking and deposition behavior of supercritical hydrocarbon aviation fuels," Combust. Sci. Technol. **178**, 307-334 (2006).
[2] J. C. Oefelein, "Mixing and combustion of cryogenic oxygen-hydrogen shear-coaxial jet flames at supercritical pressure," Combust. Sci. Technol. **178**, 229-252 (2006).
[3] T. Schmitt, L. Selle, A. Ruiz, and B. Cuenot, "Large-eddy simulation of supercritical-pressure round jets," AIAA J. **48**(9), 2133-2144 (2010).
[4] N. Zong and V. Yang, "Cryogenic liquid jets and mixing layers in transcritical and supercritical environments," Combust. Sci. Technol. **178**, 193-227 (2006).
[5] N. Okong'o and J. Bellan, "Consistent large eddy simulation of a temporal mixing layer laden with evaporating drops. Part 1: Direct numerical simulation, formulation and *a priori* analysis," J. Fluid Mech. **499**, 1-47 (2004).
[6] B. Chehroudi, D. Talley, and E. Coy, "Visual characteristics and initial growth rates of round cryogenic jets at subcritical and supercritical pressures," Phys. Fluids **14**(2), 850-861 (2002).
[7] E. Masi, J. Bellan, K. Harstad, and N. Okong'o, "Multi-species turbulent mixing under supercritical-pressure conditions: Modeling, direct numerical simulation and analysis revealing species spinodal decomposition," J. Fluid Mech. **721**, 578-626 (2013).

[8] N. Okong'o and J. Bellan, "Direct numerical simulation of a transitional supercritical binary mixing layer: Heptane and nitrogen," J. Fluid Mech. **464**, 1-34 (2002).
[9] N. Okong'o, K. Harstad, and J. Bellan, "Direct numerical simulations of O_2/H_2 temporal mixing layers under supercritical conditions," AIAA J. **40**(5), 914-926 (2002).
[10] M. Oschwald and A. Schik, "Supercritical nitrogen free jet investigated by spontaneous Raman scattering," Exp. Fluids **27**, 497-506 (1999).
[11] M. Oschwald, A. Schik, M. Klar, and W. Mayer, "Investigation of coaxial LN2/GH2-injection at supercritical pressure by spontaneous Raman scattering," AIAA Paper No. 99-2887 (1999).
[12] L. C. Selle, N. A. Okong'o, J. Bellan, and K. G. Harstad, "Modeling of subgrid scale phenomena in supercritical transitional mixing layers: An *a priori* study," J. Fluid Mech. **593**, 57-91 (2007).
[13] E. S. Taşkinoğlu and J. Bellan, "*A posteriori* study using a DNS database describing fluid disintegration and binary-species mixing under supercritical pressure: Heptane and nitrogen," J. Fluid Mech. **645**, 211-254 (2010).
[14] E. S. Taşkinoğlu and J. Bellan, "Subgrid scale models and large eddy simulation of oxygen stream disintegration and mixing with a hydrogen or helium stream at supercritical pressure," J. Fluid Mech. **679**, 156-193 (2011).
[15] D. Carati, G. Winckelmans, and H. Jeanmart, "On the modelling of the subgrid-scale and filtered-scale stress tensors in large-eddy simulation," J. Fluid Mech. **441**(14), 119-138 (2001).
[16] S. B. Pope, *Turbulent Flows* (Cambridge University Press, 2000).
[17] A. Ern and V. Giovangigli, *Multicomponent Transport Algorithms* (Springer Verlag, 1994).
[18] K. G. Harstad and J. Bellan, "Mixing rules for multicomponent mixture mass diffusion coefficients and thermal diffusion factors," J. Chem. Phys. **120**(12), 5664-5673 (2004).
[19] J. Hirshfelder, C. Curtis, and R. Bird, *Molecular Theory of Gases and Liquids* (John Wiley and Sons, 1964).
[20] A. Ern and V. Giovangigli, "Thermal diffusion effects in hydrogen-air and methane-air flames," Combust. Theory Modell. **2**, 349-372 (1998).
[21] N. Okong'o and J. Bellan, "Consistent boundary conditions for multicomponent real gas mixtures based on characteristic waves," J. Comput. Phys. **176**, 330-344 (2002).
[22] G. K. Batchelor, *An Introduction to Fluid Dynamics* (Cambridge University Press, 1999).
[23] C. Kennedy and M. Carpenter, "Several new numerical methods for compressible shear layer simulations," Appl. Numer. Math. **14**, 397-433 (1994).
[24] S. M. Muller and D. Scheerer, "A method to parallelize tridiagonal solvers," Parallel Comput. **17**, 181-188 (1991).
[25] A. I. Olemskoĭ, E. A. Toropov, and I. A. Sklyar, "Self-consistent theory of the transition of an unstable thermodynamic system from spinodal to heterophase kinetics," Sov. Phys. JETP **73**(3), 545-551 (1991).
[26] R. W. Balluffi, S. M. Allen, and W. C. Carter, *Kinetics of Materials* (John Wiley & Sons, Inc., 2005).
[27] I. A. Hannoun, H. J. S. Fernando, and E. J. List, "Turbulence structure near a sharp density interface," J. Fluid Mech. **189**, 189-209 (1988).
[28] E. B. Nauman and D. Q. He, "Nonlinear diffusion and phase separation," Chem. Eng. Sci. **56**, 1999-2018 (2001).
[29] Y. Zhang, *Geochemical Kinetics* (Princeton University Press, 2008).
[30] B. J. Cantwell, "On the behavior of velocity gradient tensor invariants in direct numerical simulations of turbulence," Phys. Fluids A **5**(8), 2008-2013 (1993).
[31] T. Leung, N. Swaminathan, and P. A. Davidson, "Geometry and interaction of structures in homogeneous isotropic turbulence," J. Fluid Mech. **710**, 453-481 (2012).
[32] V. Sahni, B. S. Sathyaprakash, and S. F. Shandarin, "Shapefinders: A new shape diagnostic for large-scale structure," Astrophys. J. Lett. **495**, L5-L8 (1998).
[33] J. V. Sheth, V. Sahni, S. F. Shandarin, and B. S. Sathyaprakash, "Measuring the geometry and topology of large-scale structure using SURFGEN: Methodology and preliminary results," Mon. Not. R. Astron. Soc. **343**, 22-46 (2003).
[34] J. V. Sheth and V. Sahni, "Exploring the geometry, topology and morphology of large scale structure using Minkowski functionals," Current Science **88**(7), 1101-1116 (2005).
[35] T. Lewiner, H. Lopes, A. W. Vieira, and G. Tavares, "Efficient implementation of marching cubes' cases with topological guarantees," J. Graphics Tools **8**, 1-15 (2003).
[36] W. E. Lorensen and H. E. Cline, "Marching cubes: A high resolution 3D surface construction algorithm," in *Proceedings of the 14th Annual Conference on Computer Graphics and Interactive Techniques* (ACM, 1987), Vol. 21, pp. 163-169.
[37] S. R. de Groot and P. Mazur, *Non-Equilibrium Thermodynamics* (Dover Publication, Inc., 1984).
[38] V. Giovangigli, L. Matuszewsky, and F. Dupoirieux, "Detailed modeling of planar transcritical H_2-O_2-N_2 flames," Combust. Theory Modell. **15**, 141-182 (2011).
[39] J. Keizer, *Statistical Thermodynamics of Nonequilibrium Processes* (Springler-Verlag, New York, 1987).
[40] J. Bardina, J. H. Ferziger, and W. C. Reynolds, "Improved subgrid scale models for large eddy simulation," AIAA Paper No. 80:80-1357 (1980).
[41] M. Germano, U. Piomelli, P. Moin, and W. H. Cabot, "A dynamic subgrid-scale eddy viscosity model," Phys. Fluids A **3**(7), 1760-1765 (1991).
[42] K. Lilly, "A proposed modification of the Germano subgrid-scale closure method," Phys. Fluids A **4**, 633 (1992).
[43] B. Vreman, B. Geurts, and H. Kuerten, "Large-eddy simulation of the turbulent mixing layer," J. Fluid Mech. **339**, 357-390 (1997).
[44] B. Vreman, B. Geurts, and H. Kuerten, "On the formulation of the dynamic mixed subgrid scale model," Phys. Fluids **6**, 4057 (1994).
[45] R. C. Reid, J. M. Prausnitz, and B. E. Polling, *The Properties of Gases and Liquids*, 4th ed. (McGraw-Hill Book Company, 1987).
[46] K. G. Harstad and J. Bellan, "High-pressure binary mass-diffusion coefficients for combustion applications," Ind. Eng. Chem. Res. **43**(2), 645-654 (2004).